

1 Comparison of ocean heat content from two eddy-resolving 2 hindcast simulations with OFES1 and OFES2

3 Fanglou Liao^{1,2}, Xiao Hua Wang^{2*} and Zhiqiang Liu^{1,3*}

4 ¹Department of Ocean Science and Engineering, Southern University of Science and Technology, Shenzhen, 518055,
5 China

6 ²The Sino-Australian Research Consortium for Coastal Management, School of Science, The University of New South
7 Wales, Canberra, 2610, Australia

8 ³Southern Marine Science and Engineering Guangdong Laboratory (Guangzhou), Guangzhou, 511458, China

9 *Correspondence to:* Zhiqiang Liu (liuzq@sustech.edu.cn) or Xiao Hua Wang (x.h.wang@unsw.edu.au)

10 **Abstract.** The ocean heat content (OHC) estimates from eddy-resolving hindcast simulations from the Ocean General
11 Circulation Model for the Earth Simulator Version 1 (OFES1) and Version 2 (OFES2), and a global objective analysis
12 of subsurface temperature observations (EN4) were compared. OHC increased in most of the global ocean above 2000
13 m in the EN4 and OFES1 over 1960–2016, mainly a result of deepening of neutral density surfaces, with variations
14 along the neutral density surfaces of regional importance. We found substantial differences in the temporal and spatial
15 distributions of the OHC between the two OFES hindcasts, especially in the Atlantic Ocean. A basin-wide heat budget
16 analysis showed that there was less surface heating for the major basins in the OFES2. The horizontal heat advection
17 was largely similar but the OFES2 had a much stronger meridional heat advection associated with the Indonesian
18 Throughflow (ITF) above 300 m. Also, large discrepancies in the vertical heat advection based on the two OFES data
19 were also identified, especially at the 300 m in the Indian Ocean. Therefore, we concluded that there exist large
20 discrepancies in the inferred vertical heat diffusion (cannot be directly diagnosed in this paper due to data availability),
21 which, along with the different sea surface heat flux and vertical heat advection, were the major factors responsible
22 for the examined OHC differences. This work may be a useful reference for future OFES users.

23 1 Introduction

24 The global ocean has stored over 90% of the extra heat added to the Earth system since 1955, causing a significant
25 increase in the ocean heat content (OHC) (Levitus et al., 2012; IPCC 2013). The OHC is therefore an important
26 indicator of climate change, and provides useful bounds in estimating the Earth's energy imbalance (Palmer et al.,
27 2011; Von Schuckmann et al., 2016). Although natural factors such as the El Niño–Southern Oscillation (ENSO) and
28 volcanic eruptions can affect the OHC (Balmaseda et al., 2013; Church et al., 2005), the recent warming has mostly
29 resulted from greenhouse gases accumulating in the atmosphere (Abraham et al., 2013; Gleckler et al., 2012; Pierce
30 et al., 2006).

31 A major concern in both the oceanography and climate communities, the OHC has attracted a great deal of
32 attention. Although direct observational records are the most trustworthy data in determining the oceanic thermal state,
33 the fact is that measurements are far from dense enough in both the temporal and spatial domains, especially for the
34 deep and abyssal oceans. This situation has greatly improved since the launch of a global array of profiling floats, the

35 Argo, in 2000s. However, the spatial resolution of the Argo program of approximately 300 km is not able to capture
36 mesoscale structures (Sasaki et al., 2020, hereafter S2020). Several approaches exist to fill the temporal and spatial
37 gaps in global temperature measurements, and can be used to produce gridded temperature fields to estimate the OHC.
38 These approaches include the objective analysis of observational data and ocean reanalysis combining physical ocean
39 models with observations. In addition, ocean general circulation models (OGCMs) provide temperature fields by
40 solving the primitive equations of fluid motion and state. Although OGCMs are dynamically consistent (the resulting
41 fields satisfy the underlying fluid dynamics and thermodynamics equations), some are not constrained by observations.
42 How multi-scale dynamical processes are represented in these unconstrained models and their implementation of
43 external forcing significantly impact their OHC estimates.

44 The Ocean General Circulation Model for the Earth Simulator (OFES; Masumoto et al., 2004; Sasaki et al., 2004),
45 developed by the Japan Agency for Marine-Earth Science and Technology (JAMSTEC) and other institutes, is a well-
46 known eddy-resolving ocean model, and the hindcast simulation of the OFES Version 1 (OFES1) has been widely
47 used (Chen et al., 2013; Dong et al., 2011; Du et al., 2005; Sasaki et al., 2020; Wang et al., 2013). The hindcast
48 simulation based on the OFES Version 2 (OFES2) has now been released, and certain improvements have been
49 demonstrated over the OFES1 (S2020). For example, the authors found smaller bias in the global sea surface
50 temperature (SST), sea surface salinity (SSS) and the water mass properties in the Indonesian and Arabian Seas. To
51 our knowledge, however, a comparison of the multi-decadal OHC at a global scale from the OFES1 and OFES2 is
52 lacking. As this high-resolution quasi-global model is expected to be widely used in the oceanography and climate
53 communities for examining the ocean state in the near future, it is necessary to compare the OHC estimates from these
54 two OFES versions as an indicator of the potential improvements in the OFES2 over the OFES1, and also of their
55 adaptability to the OHC-related studies. This is further motivated by the finding that subsurface oceanic fields could
56 be notably different between the results of two OFES runs with different atmospheric forcing, despite their results in
57 the near-surface may be similar (Kutsuwada et al., 2019).

58 The aim of this paper is twofold: (1) to estimate the OHC in the global ocean and each major basin using the OFES1
59 and OFES2, with primary focus on their differences; (2) to understand the causes of the differences between these two
60 simulations. To this end, we used the potential temperature θ to calculate the OHC from 1960 to 2016 for both the
61 global ocean and the major basins, the Pacific Ocean, the Atlantic Ocean and the Indian Ocean, between 64° S and
62 64° N.

63 In Section 2, we give a brief description to the data and methods used here. In Section 3, we describe and discuss
64 the OHC differences between the datasets in both the temporal and spatial domains. A tentative analysis of the possible
65 causes of the differences is also conducted. Sections 4 summarises the principal points and possible extensions
66 involving factors that were not examined here due to data availability but could be important. Future work is therefore
67 expected to improve on our work here.

68
69

70 **2 Data and Methods**

71 **2.1 Data**

72 Potential temperature θ from both the OFES1 and OFES2 were used to calculate the global and basin OHCs for
73 comparison with each other and with the OHC calculated from the observation-based EN4. Although results from the
74 EN4 cannot be taken as the actual oceanic state, it has been widely used in OHC-related studies (Allison et al., 2019;
75 Carton et al., 2019; Häkkinen et al., 2016; Trenberth et al., 2016; Wang et al., 2018). A brief description of the three
76 datasets is given below; readers are referred to Sasaki et al. (2004), Sasaki et al. (2020) and Good et al. (2013) for
77 more details.

78 The OFES1 has a horizontal spatial resolution of 0.1° and 54 vertical levels with a maximum depth of 6065 m
79 (Sasaki et al., 2004); this high lateral resolution enables it to resolve mesoscale processes. Following a 50-year
80 climatological simulation, the hindcast simulation of the OFES1 was integrated from 1950 to two years ago (the
81 publically available data is till 2017). The multi-decadal integration period makes it possible to perform an analysis
82 of oceanic fields at temporal scales from intraseasonal to multi-decadal. Unlike most other datasets used for OHC
83 estimates, the OFES1 is an ocean modelling with no observational constraints. Therefore, it can be used to demonstrate
84 the potential benefits of high resolution and the adaptability of numerical modelling without data assimilation.

85 The OFES2 has the same horizontal spatial resolution of 0.1° . Vertically, there are 105 levels, with a maximum
86 depth of 7500 m. The OFES1 uses daily National Centers for Environmental Prediction (NCEP) reanalysis ($2.5^\circ \times$
87 2.5° ; Kalnay et al., 1996) for the atmospheric forcing, whereas the OFES2 is forced by the 3-hourly atmospheric
88 surface dataset JRA55-do Version 08 ($55\text{km} \times 55\text{km}$; Tsujino et al., 2018). Both the temporal and spatial resolutions
89 of the atmospheric forcing have increased greatly in the OFES2. The OFES2 also incorporates river runoff and sea-
90 ice models, although no inclusion of polar areas.

91 In the horizontal direction, both the OFES1 and OFES2 use a biharmonic mixing scheme to suppress computational
92 noise (S2020). The horizontal diffusivity coefficient is equal to $-9 \times 10^9 \text{ m}^4/\text{s}$ at the Equator (S2020), and varies
93 proportional to the cube of the cosine of the latitude (personal communication with Hide Sasaki) and. The OFES2
94 uses a mixed-layer vertical mixing scheme (Noh and Jin Kim 1999) with parametrization of tidal-energy dissipation
95 (Jayne and St. Laurent 2001; St. Laurent et al., 2002), whereas the OFES1 uses the K-profile parameterization (KPP)
96 scheme (Large et al., 1994). With the temperature and salinity on 1st January 1958 from the OFES1 as the initial
97 conditions, the OFES2 used here has been integrated from 1958 to 2016. To reduce the computation and archive cost,
98 we subsampled the OFES1 and OFES2 data every 5 grid points in the horizontal direction.

99 To evaluate the OHC objectively from the two OFES data, we used the EN4 from the UK Meteorological Office
100 Hadley Centre as a reference. The EN4 data can be considered as an objective analysis that is primarily based on
101 observations (Good et al., 2013), with a horizontal resolution of 1° and 42 vertical levels down to 5350 m. The EN4
102 assimilates data mainly from the World Ocean Database (WOD) and the Coriolis dataset for ReAnalysis (COR).
103 Pre-processing and quality checks are conducted before the observational data are used to construct this objective
104 analysis product.

105 Although we use the EN4 results as a reference for evaluating the OFES performance in simulating the 57-year
106 ocean thermal state, the EN4 cannot be taken as the actual ocean state. The main reason is that the measurements used

107 to construct the EN4 datasets are sparse and inhomogeneous in both the temporal and spatial domains, and far from
 108 sufficient to resolve mesoscale or even sub-mesoscale motions. There are more observations in the Northern
 109 Hemisphere than in the Southern Hemisphere, and there is also a seasonal bias in the observational data density
 110 (Abraham et al. 2013; Smith et al. 2015). A higher density of records became available only after the World Ocean
 111 Circulation Experiment (WOCE) in the 1990s and launch of the Argo profiling floats in the 2000s. Table 1 summarizes
 112 these three ocean datasets.

113

114 **Table 1.** Description of the OFES1, OFES2 and EN4 datasets. / means not applicable.

	OFES1	OFES2	EN4
Model	MOM3	MOM3	/
Horizontal coverage	75° S – 75° N	76° S – 76° N	83° S – 89° N
Grids	3600 × 1500	3600 × 1520	360 × 173
Maximum depth	6065 m	7500 m	5350 m
Vertical levels	54	105	42
Atmospheric forcing	Daily NCEP/ NCAR reanalysis	3-hourly JRA55-do Ver.08	/
Data assimilated			WOD, CORA
Time span	1950 – 2017	1958 – 2016	1900 – 2021

115

116 We considered water from the sea surface to around 2000 m and divided it into three layers: upper (0–300 m);
 117 middle (300–700 m); and lower (700–2000 m). The ocean above 2000 m has often been divided into two layers, 0–
 118 700 m and 700–2000 (or even one: 0–2000 m) (Allison et al., 2019; Hakkinen et al., 2016; Häkkinen et al., 2015;
 119 Levitus et al., 2012; Zanna et al., 2019); our analysis here will show that it is in fact necessary to divide it into three
 120 layers for our purpose, as did Liang et al. (2021). The temperature and salinity characteristics of the upper ocean,
 121 above 300 m, were also analysed in Carton et al. (2018, 2019).

122 The reasons for ignoring water below 2000 m are mainly fourfold. Firstly, the simulated behaviour of the deep
 123 ocean depends sensitively on the spin-up of the numerical simulation, which is almost always incomplete (Wunsch
 124 2011), at least in the first decade. Secondly, the observational data used in the EN4 are largely confined to the ocean
 125 above 2000 m (many available measurements do not even go down this deep), with a much lower density of data in
 126 the deep and abyssal oceans. Thirdly, the data in the EN4 version that we used here are bias-corrected, following
 127 Levitus et al. (2009), in which only the ocean above 700 m was considered. Therefore, for instance, the Expendable
 128 Bathythermograph (XBT) profiles below 700 m are corrected using the correction values provided for 700 m (personal
 129 communication from the Meteorology Office Hadley Centre). Lastly, as can be seen, the maximum depth differs by
 130 more than 2000 m between the OFES2 and EN4. It was felt that a full-depth OHC is not highly comparable between
 131 the three datasets. This, however, does not imply that the deep ocean can be ignored; it can play an essential role in
 132 regulating the global-ocean thermal state (Desbruyeres et al. 2016; Desbruyères et al. 2017; Palmer et al. 2011). It is
 133 expected that a much better understanding of the deep and abyssal ocean state will be gained with the implementation
 134 of the Deep Argo program.

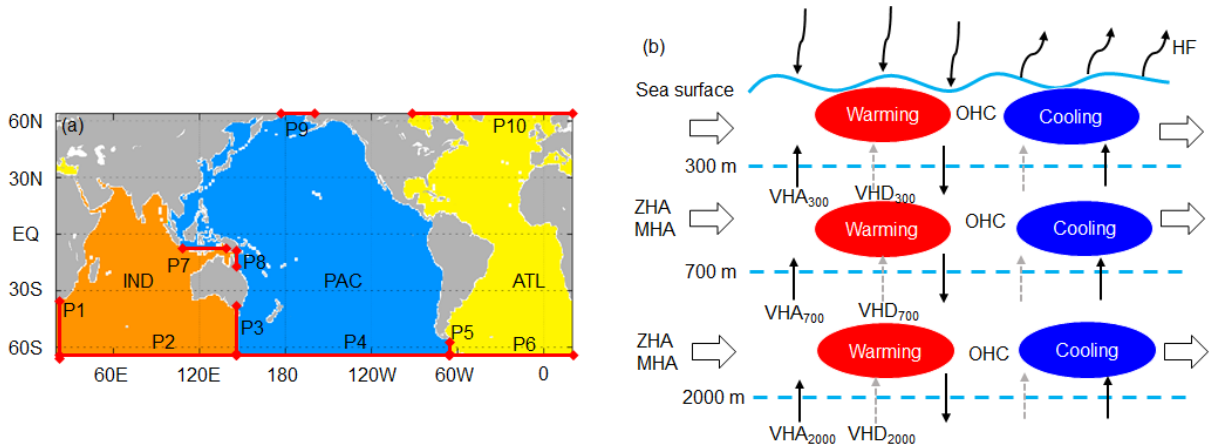
135 **2.2 Methods**

136 We compared the three datasets over the period 1960–2016. Following convention, the OHC values here are the OHC
 137 anomalies relative to estimates in 1960. At each grid point, the OHC is given by

138
 139
$$\text{OHC} = \rho \delta v C_p (\theta - \theta_{1960}) = \rho \delta v C_p \Delta \theta, \quad (1)$$

140 where ρ is the seawater density (kg/m), δv the grid volume (m³), C_p the specific heat of seawater at constant pressure
 141 (J/kg/°C), θ the yearly potential temperature (°C) and θ_{1960} the averaged potential temperature in 1960. The total
 142 OHC in the upper ocean layer (above 300 m) is the integral of Eq. (1) from 0 to 300 m. Similar procedures apply to
 143 the other two layers. A value of 4.1×10^6 kg·J/m³/°C was used for the product of ρ and specific heat of seawater C_p
 144 (Palmer et al., 2011).

145 Both the global and individual-basin OHCs were calculated for comparison. Fig. 1 shows the domains of the Pacific,
 146 Atlantic and Indian Oceans between 64° S and 64° N, with their respective marginal seas included. The definition of
 147 the marginal seas of the Pacific and Indian Oceans may be inconsistent with some other studies. The major water
 148 passages connecting the different basins are also labelled in Fig. 1a. A schematic diagram shows the primary processes
 149 determining the OHC of an ocean basin (Fig. 1b).



150
 151 **Figure 1.** Domains of the major basins between 64° S and 64° N and a schematic diagram of the primary processes controlling the
 152 thermal state of an ocean. (a) The PAC stands for the Pacific Ocean, the ATL for the Atlantic Ocean and the IND for the Indian
 153 Ocean. The basin domain is extracted using the gcmfaces package (Forget et al., 2015) and then interpolated to the corresponding
 154 grid of each product. Grey indicates the land. The red solid lines with diamond arrow stand for the water passage connecting
 155 different basins. We label it with the capital letter P (abbreviation for passage) and a serial number. EQ stands for the Equator. (b)
 156 We use a light blue curve to represent the wave-shaped sea surface and three dashed lines to indicate the 300 m, 700 m and 2000
 157 m depth. The curve arrow represents the net heat flux (HF) through the ocean surface. The black hollow arrows show the zonal
 158 (ZHA) or meridional (MHA) heat advection. The black thin arrow represents the vertical heat advection (VHA) and the grey dash
 159 arrow stands for the vertical heat diffusion (VHD). The red ellipse illustrates warming water and the blue ellipse cooling water. P1:
 160 (20° E, 64° S – 34.5° S); P2: (20° E – 146.5° E, 64° S); P3: (147° E, 64° S – 36.5° S); P4: (147° E – 65.5° W, 64° S); P5: (67° W,
 161 64° S – 55° S); P6: (65° W – 19.5° E, 64° S); P7: (118.5° E – 138.5° E, 8.5° S); P8: (142° E, 12.5° S – 8° S); P9: (172.5° W – 166.5°
 162 W, 64.5° N); P10: (88° W – 24.5° E, 64.5° N).

163
 164 In addition, the $\Delta \theta$ at a fixed depth are decomposed into a heave (HV component (second term in Eq. (2) below)
 165 and a spice (SP) component (third term in Eq. (2)) (Bindoff and McDougall 1994). The HV-related warming or cooling
 166 is a result of vertical displacement of the neutral density surfaces (a continuous analogue of discretely referenced

167 potential density surfaces; [Jackett and McDougall, 1997](#)). In general, both the dynamical changes and the change in
 168 the renewal rates of water masses can induce vertical displacement and thus the HV-related warming or cooling as a
 169 consequence ([Bindoff and McDougall, 1994](#)). The SP represents warming or cooling as a result of density
 170 compensation in the θ and salinity (S) along the neutral density surfaces. This decomposition of $\Delta\theta$ helps to better
 171 understand the contributions and ways of different water masses in accounting for the OHC. The formula decomposing
 172 the potential temperature is

$$173 \quad d\theta/dt|_z = - \overbrace{dz/dt|_n}^{\text{HV}} d\theta/dz + \overbrace{d\theta/dt|_n}^{\text{SP}} \quad (2)$$

174 where t is the time (year), z means the depth (m) and $|_n$ means along the neutral density surface.

175 A program by [Jackett and McDougall \(1997\)](#) was used to calculate the neutral densities, HV and SP, this code is
 176 based on the UNESCO (The United Nations Educational, Scientific and Cultural Organization) 1983 for the
 177 computation of fundamental properties of seawater ([http://www.teos-
 178 10.org/preteos10/software/neutral_density.html](http://www.teos-10.org/preteos10/software/neutral_density.html)); we used its Matlab version. The main inputs for this program are
 179 the θ and S . As the code limits the latitude to between 80° S and 64° N, we further confine our investigation domain
 180 to be 64° from the equator; this also avoids comparisons in sea-ice impacted areas, knowing that only the OFES2
 181 includes a sea-ice model.

182 To analyze the causes of OHC differences from thermodynamic and dynamic perspectives, we calculated the
 183 surface heat flux (HF), zonal heat advection (ZHA), meridional heat advection (MHA) and vertical heat advection
 184 (VHA). Owing to a temporary suspension of the OFES2 data by the JAMSTEC, we could not access the vertical
 185 diffusivity data of the OFES2 (OFES1 does not provide these data) when preparing this manuscript. This prevents us
 186 to directly comparing the vertical diffusion of heat from the OFES1 and OFES2. Alternatively, we calculated the
 187 residual of the total OHC and all the other heat inputs (HF, ZHA, MHA and VHA), and took this as a proxy for the
 188 vertical diffusion. As the horizontal heat diffusion was found to be much weaker than the ZHA and MHA (not shown),
 189 we did not include it in the analysis. A diagram of the primary processes is shown in Fig. 1b.

190 **3 Results**

191 The principal aim here is to compare the results from the OFES1 and OFES2, with the EN4 acting as an observation-
 192 based reference. If there was a significant difference between the OFES2 result and that of one or both of the other
 193 two datasets, does this represent a real phenomenon not present in the other two widely used datasets or is it an
 194 unwanted property of the newly released OFES2 simulation? In this section, we compare the three sets of results for
 195 the global ocean, and for each of the Pacific, Atlantic and Indian Oceans individually.

196 **3.1 Time evolution of the OHC, HV and SP from 1960 to 2016**

197 **3.1.1 The time series of OHC, HV and SP**

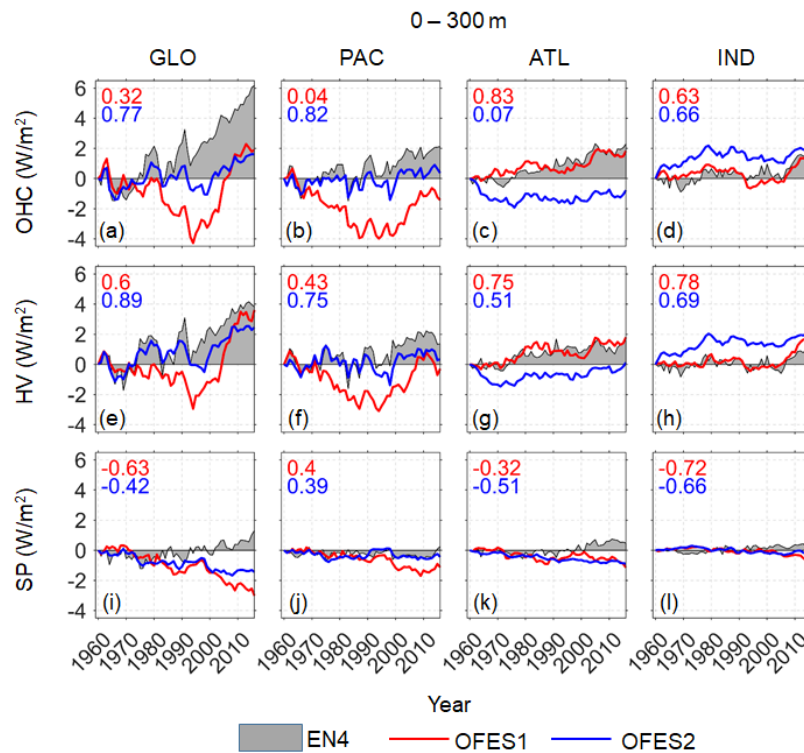
198 Figs. 2–4 present the time series of the total OHC, and its HV and SP components for the upper (0–300 m), middle
 199 (300–700 m) and lower (700–2000 m) ocean layer, respectively. Note that OHC, HV and SP were calculated as the

200 anomaly relative to the estimates in 1960, and converted to an equivalent heat flux applying over the entire surface
 201 area of the Earth, as suggested by one reviewer.

202

203 *Upper layer*

204 For the global ocean between 0–300 m, all three data indicate cooling from around 1963 to 1966 (Fig. 2a), explained
 205 as the result of the volcanic eruption of Mount Agung (Balmaseda et al. 2013). A similar cooling over this period can
 206 also be seen in Domingues et al. (2008) and Allison et al. (2019) for the upper 700 m (their Fig. 1) and Achutarao et
 207 al. (2007) for both the 0–700 m and 0–3000 m (their Fig. 1). This short but sharp cooling was found to mainly impact
 208 the Pacific Ocean (Fig. 2b). Marked OHC reductions associated with the strong volcanic eruptions of El Chichón in
 209 1982 (a strong ENSO also emerged in 1982–83) and Pinatubo in 1991 were also consistently captured by all the three
 210 data.



211

212 **Figure 2.** Time series of the global and basin-wide OHC (top), HV (middle) and SP (bottom) between 0–300 m based on the
 213 three temperature products. The OHC, HV and SP here are converted to the accumulative heating in $W \cdot m^{-2}$ applied over the entire
 214 surface of Earth. Grey shadow: EN4; red solid line: OFES1; blue solid line: OFES2. Numbers on the left top corners are the
 215 correlation coefficients between the OFES1 (red) or OFES2 (blue) and EN4. The OHC hereafter is directly calculated from the
 216 potential temperature, rather than the sum of the HV and SP.

217

218 Both the EN4 and OFES2, but not the OFES1, showed a slowdown in warming and even cooling in the Pacific
 219 Ocean during the 2000s. This slowdown in Pacific warming corresponded to a sharp warming in the upper layer of
 220 the Indian Ocean. This relevance between the Pacific and Indian Ocean was found to be a consequence of an
 221 intensifying Indonesian Throughflow, leading to an increased heat transport from the Pacific to the Indian Oceans
 222 (Lee et al. 2015; Zhang et al. 2018); however, these two references considered the top 700 m. As will be shown,

223 however, this sudden warming of the Indian Ocean was largely confined to the above 300 m, especially as indicated
224 by the OFES1 and OFES2 (Fig. 3d). The EN4 showed a clear warming acceleration around 2003 in the global ocean
225 above 300 m, which was probably an artefact of the transition of the ocean observation network from a ship-based
226 system to Argo floats (Cheng and Zhu, 2014), although these authors mainly used subsurface temperature data from
227 the World Ocean Database 2009 (WOD09). Interestingly, a dramatic shift can also be seen in the OFES1 (Fig. 2a),
228 remembering that the OFES1 is not directly constrained by observations. A major difference in this jump between the
229 EN4 and OFES1 is that it was found to be more closely associated with the SP in the EN4 (Fig. 2i) but with the HV
230 in the OFES1 (Fig. 2e). This spiciness warming around 2003, derived from objective analysis of observational data
231 can serve as a complement of the work by Cheng and Zhu (2014).

232 However, many significant differences can be found between the three datasets. The EN4 indicated an
233 approximately linear warming since 1970 (Fig. 2a), modulated by the abovementioned climate signals. The OFES1,
234 however, showed that the cooling persisted almost until the beginning of the 1990s, when a similar linear but stronger
235 warming appeared afterwards (Fig. 2a); this is more than 20 years later than that indicated by the EN4. The
236 approximately linear warming appeared even later in the OFES2 from around 2000, and was the weakest among the
237 three datasets.

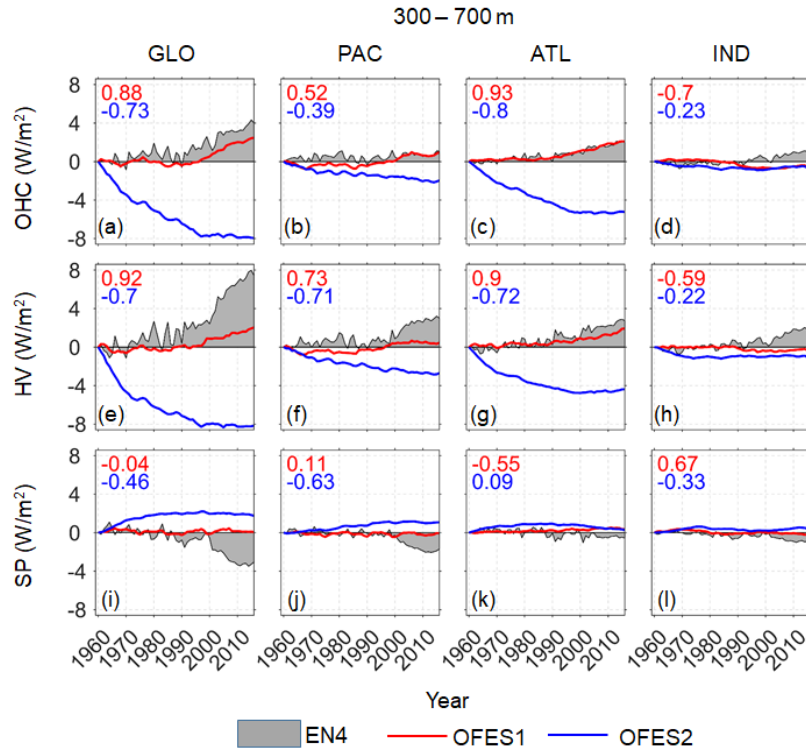
238 Compared to the OFES1, the OFES2 agreed better with the EN4 in the temporal profile of the global ocean (Fig.
239 2a), which, to some extent, is consistent with the smaller sea surface temperature (SST) bias from the OFES2 than
240 that from the OFES1 when comparing to the World Ocean Atlas 2013 (WOA13) (S2020). However, there was a large
241 magnitude difference after 1980. This came mainly from the spiciness component (Fig. 2i), with both the OFES1 and
242 OFES2 indicating clear SP cooling. This may imply some discrepancies in the salinity characteristics from these three
243 data. In contrast, there was quite good agreement in the HV from the EN4 and OFES2 (Fig. 2e).

244 Clear differences can also be easily discerned for each individual basin. The OFES1 differed significantly from the
245 other two in the Pacific Ocean between around 1970–1990, with the other two similar to each other in both the HV
246 and SP. In the Atlantic Ocean, however, the OFES1 agreed with the EN4 quite well in the HV. Although the two
247 OFES datasets had similar spiciness in the Atlantic Ocean, they both disagreed with the spiciness from the EN4. The
248 HV indicated by the OFES2 showed poor agreement with both the EN4 and OFES1 in the 1960s (Fig. 2g). In the
249 Indian Ocean, the OFES1 was much closer to the EN4 than the OFES2. Both the similarities and differences in the
250 OHC came largely from the HV, which dominates the variation of OHC. The notable deviations of the OFES2 relative
251 to others mainly come from the uniquely strong warming in the OFES2 Indian Ocean before around 1980 (Fig. 2d).

252 A potential issue of the OFES2 is the spin-up, although it started from the calculated the temperature and salinity
253 fields. Without a knowledge about when it is fully spun-up, we here show and compare its simulated results starting
254 from 1960, only excluding the first two years (1958–1959). It seems that the OFES2 has a good agreement with the
255 EN4 since around 1970s in both the Atlantic and Indian Oceans (Fig. 2c, d), which is likely to be related to the better
256 spun-up with time. However, in the Pacific Ocean, the OFES2 was quite similar to the EN4 before 1990, especially
257 in the HV component. This to some extent, may weaken the spin-up argument.

258
259 *Middle layer*

260 In the middle ocean layer (300–700 m) (Fig. 3), there were remarkable differences in the OHC and its HV and SP
 261 components between the OFES2 and the other two datasets, most noticeable for the global ocean and the Atlantic
 262 Ocean, less so for the Pacific Ocean; there was little difference for the Indian Ocean. The OFES2 showed a moderate
 263 Pacific cooling for almost the whole 57-year period and a strong Atlantic cooling trend until around 2000, with a
 264 subsequent hiatus in the Atlantic Ocean. There was a minor Indian cooling from the OFES2 in the 1960–70s. In the
 265 OFES2, this cooling was mainly due to the decreasing HV, as its spiciness was largely more positive than the other
 266 two.



267
 268 **Figure 3.** As for Fig.2 but for the middle layer (300–700 m).
 269

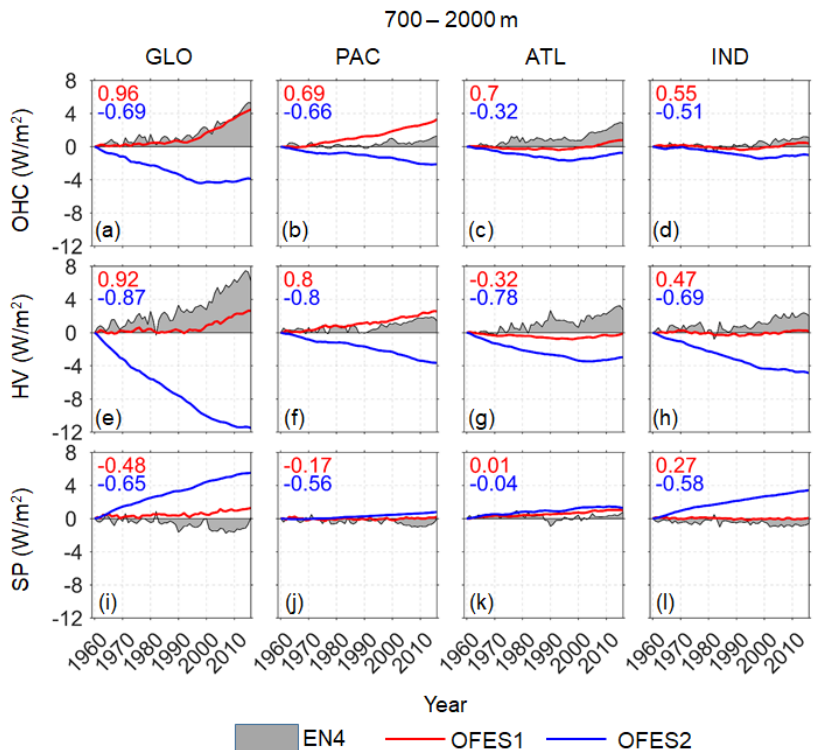
270 In contrast, both the EN4 and OFES1 indicated that this layer was relatively stable before about 1990. Then, the
 271 EN4 and the OFES1 both showed the global ocean and the Atlantic Ocean warming (Fig. 3a, c), mostly due to an
 272 increase in the HV (Fig. 3e, g). Despite this good agreement between the EN4 and OFES1, there were notable
 273 differences in their HV and SP components. Compared to the OFES1, there was a generally stronger positive HV in
 274 the EN4 (Fig. 3e–h), and a stronger but negative SP in the EN4, particularly after about 2000 (Fig. 3i, j). A possible
 275 reason for this is the fact that there have been much more observations available since the WOCE (World Ocean
 276 Circulation Experiment) in the late 1990s and from Argo since the beginning of 2000s. This may have led to a
 277 systematic trend in the observational-based dataset EN4. Unlike in the EN4 and OFES2, the SP variations in the
 278 OFES1 were almost invisible for almost all the basins. In addition, aforementioned significant warming acceleration
 279 from the early 2000s to 2010s in the Indian Ocean (Fig. 2d) can still be seen in the EN4 (Fig. 3d), but this was almost
 280 invisible in the two OFES datasets.

281 One major cause of the profound differences between the OFES2 and the EN4 is the spin-up issue. Indeed, even
 282 after 2000, clear differences remain in the global ocean. This, on the one hand, is expected because the middle layer
 283 takes more time to be well spun-up compared to the upper layer; on the other hand, suggests that special caution is
 284 needed when investigating the multi-decadal variations, or even decadal variations in the recent two decades based on
 285 the OFES2.

286
 287 *Lower layer*

288 In the lower ocean layer (700–2000 m) (Fig. 4), the OFES2 was clearly again the outlier of the three datasets. It showed
 289 that the Atlantic and Indian Oceans experienced cooling from 1960 to the end of 1990s (Fig. 4c, d), then a slight
 290 warming. The Pacific Ocean, however, was shown cooling over the whole 57-year period (Fig. 4b). The better
 291 agreement with the EN4 since the end of 1990s may be related to the spin-up issue of the OFES2, at least to some
 292 extent. However, the agreement between the EN4 and OFES2 was even better than in the middle layer (300–700 m),
 293 particularly in the Atlantic and Indian Oceans. This may weaken the spin-up argument, as it is expected that the
 294 middle layer was more easily spun-up than the lower layer.

295 The OHC variations from the OFES1 and the EN4 were much the same for the global ocean, but this was a result
 296 of the cancelling of the substantial differences in the Pacific and Atlantic Oceans (Fig. 4b, c), and in the HV and SP
 297 (Fig. 4e–l). Specifically, there was a larger OHC increase in the Pacific Ocean from the OFES1 than the EN4, but the
 298 latter showed a larger OHC increase in the Atlantic Ocean. From the perspective of potential temperature
 299 decomposition, the EN4 generally showed a stronger HV increase than the OFES1 in the Atlantic and Indian Oceans
 300 (Fig. 4g, h) but a stronger negative SP or weaker positive SP increase (Fig. 4i–l).



301
 302 **Figure 4.** As for Fig.2 but for the lower layer (700–2000 m).

303 3.1.2 Temporal evolution in the OHC, HV and SP trend

304 Figs. 2–4 show clearly the similarities and differences between the three datasets in the time series of the OHC, HV
305 and SP for the period 1960–2016; these vary with time. Therefore, in this section, we calculate the linear trend in the
306 OHC, HV and SP over a rolling window of 10 years for the three datasets, following [Smith et al. \(2015\)](#); the results
307 for the three layers are shown in Figs. 5–7, respectively. This helps to quantitatively compare the performance of these
308 data over each temporal window.

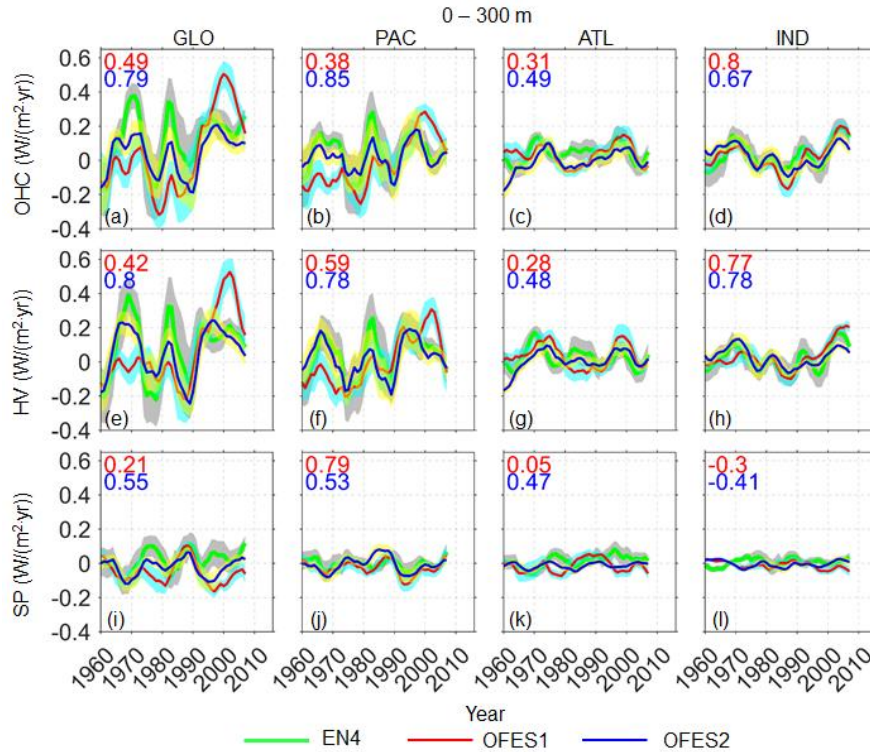
309

310 *Upper layer*

311 The datasets were similar in the profile of the OHC 10-year rolling trend; they captured most of the peaks and troughs.
312 There was better agreement in the Indian Ocean (Fig. 5d) than in the other two basins (Fig. 5b, c) but there were still
313 significant differences even in this shallow layer. The rolling trend for the global ocean from the EN4 was positive
314 most of the time, except at the beginning of the 1960s and at the ends of the 1970s and 1980s (Fig. 5a). However, the
315 OFES1 showed a cooling trend in the global ocean before around 1990; it then indicated a larger warming trend than
316 the other two. The OFES2 generally had a better agreement with the EN4 for the global ocean, but the warming trend
317 was much smaller than that from the EN4 from the late 1960s to around 1990. Since the beginning of 1990s, the trend
318 disparity between the OFES2 and the EN4 was much reduced but the OFES2 still showed a consistently weaker
319 warming trend. This better agreement may be attributed to two causes. Firstly, after around 30-years running, the
320 OFES2 was believed to have been better spun-up and therefore closer to the actual state. Secondly, it is also possible
321 that the accuracy of the EN4 data increased as more observational data were included, given that the number of
322 oceanographic observations has increased significantly since the 1990s (e.g. satellite-based SST measurements).

323 Among the differences between the three datasets, the three extreme trend peaks at around 1970, 1980 and 2000
324 (Fig. 5a) are particularly prominent, with remarkable differences between the two OFES and EN4, indicating some
325 deficiencies of numerical modelling in the reproducing of strong climate events. Apart from some minor magnitude
326 differences, the three data agreed best in the Indian Ocean (Fig. 5d). The OFES1 was close to the EN4 in showing
327 significant warming in the Indian Ocean in the 2000s, whereas the OFES2 showed a relatively weaker warming. A
328 second better agreement between the three datasets was reached in the Atlantic Ocean.

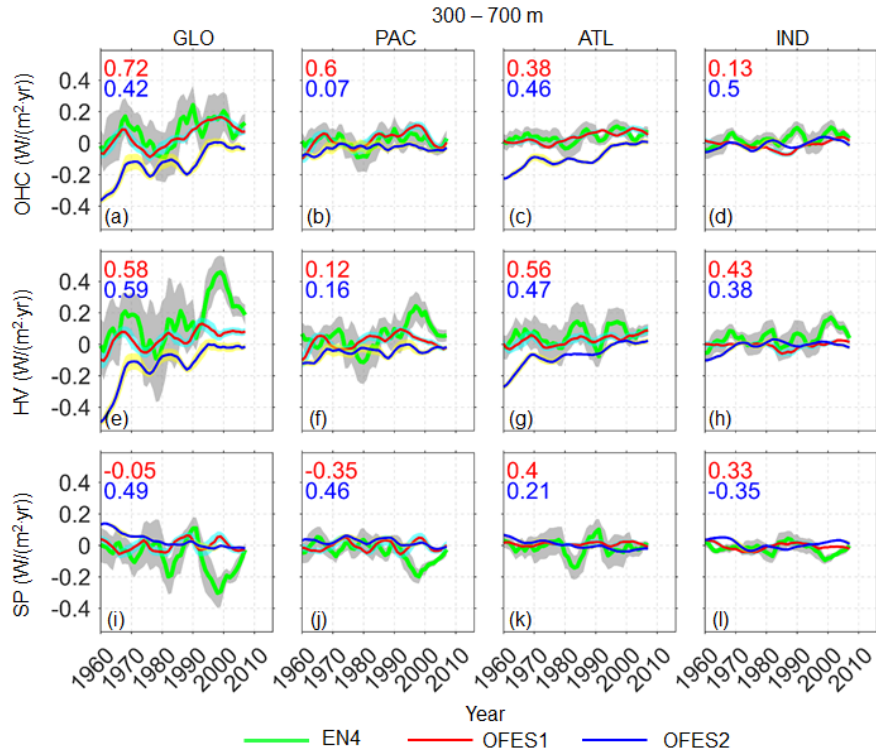
329 The HV clearly dominated the 10-year rolling trend in all basins (Fig. 5e–h), and the major differences between
330 the three datasets resulted from differences in the HV component. In addition, there was an apparent out-of-phase
331 relationship between the HV and SP trends in the global ocean and Pacific Ocean. This correspondence between the
332 HV and SP is expected for typical stratification associated with subtropical gyres (Hakkinen et al. 2016), with warm
333 and salty water over the cold and fresh water. The OFES1 and OFES2 were quite close in the simulation of spiciness,
334 particularly in the individual basins (Fig. 5i–l).



335
 336 **Figure 5.** Temporal evolution of the 10-year rolling trends in the global and basin OHCs (**top row**), HV (**middle row**) and SP (**bottom row**) in the top ocean layer (0–300 m), based on the three datasets. Numbers in the top left corners are the correlation coefficients between the EN4 and the OFES1 (red) or OFES2 (blue). The OHC, HV and SP were converted to accumulative heating (W m^{-2}) over the entire surface of the Earth. Thick green line: EN4 (grey shadow: 95% confidence interval); thin red solid line: OFES1 (cyan shadow: 95% confidence interval); thin blue solid line: OFES2 (yellow shadow: 95% confidence interval). The OHC from now on is calculated directly from the potential temperature, rather than as the sum of the HV and SP.

342
 343 *Middle layer*

344 The variation in the 10-year rolling trend from the OFES1 and the EN4 was much the same for the global, Pacific and
 345 Atlantic Oceans, but the latter dataset having a much large uncertainty. The OFES2 showed significantly different and
 346 generally cooling trend, especially concentrated in the Atlantic Ocean, consistent with Fig. 3; the reasons why notable
 347 cooling trend from the OFES2 in the Atlantic Ocean weakened with time needs a further detailed study. It was found
 348 that the cooling trend in the OHC from the OFES2 came largely from the HV. In the Pacific Ocean (Fig. 6b), the
 349 OFES2 consistently show a weak cooling trend, but in the middle and late 1960s and after around 1980, both the EN4
 350 and OFES1 showed a warming trend of similar magnitudes. The OFES1 also agreed well with the EN4 in the Atlantic
 351 Ocean, both indicating weak warming for most of the period but also sporadic cooling trend. However, these good
 352 agreements are the compensation results of the significantly different HV and SP components from the OFES1 and
 353 EN4. For example, the EN4 showed much stronger HV warming trend than the OFES1 in the Pacific Ocean since the
 354 early 1990s, but in the meantime, the EN4 also indicated strong SP cooling trend. In the Indian Ocean, the EN4
 355 presented warming trend over much of the 57-year period, whereas the two OFES datasets showed weak variations
 356 and reversals between warming and cooling.

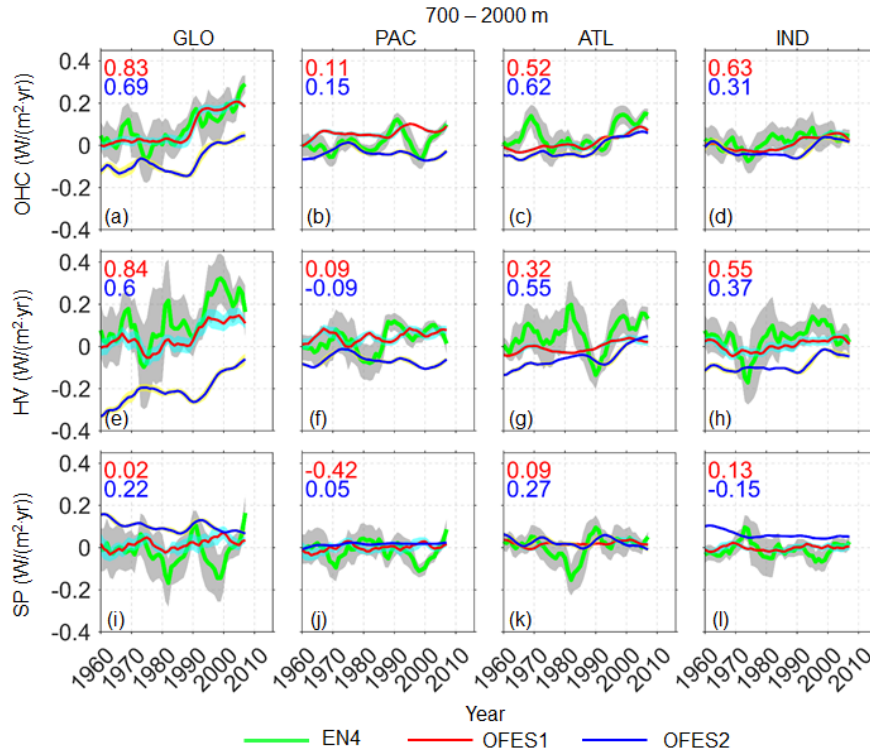


357
 358 **Figure 6.** As for Fig. 5 but for middle layer (300–700 m).
 359

360 *Lower layer*

361 As in the middle layer, the OFES2 differed significantly from other two datasets by showing a cooling trend in the
 362 global ocean until about 2000 (Fig. 7a). Although a warming trend appeared in the global ocean in the OFES2, the
 363 intensity was much lower than that of the EN4 and OFES1. The major differences between the two OFES datasets
 364 occurred in the Pacific Ocean (Fig. 7b), and was mostly HV-associated. Despite of the good agreements in the OHC
 365 trend between the OFES1 and OFES2 in the Atlantic and Indian Oceans (Fig. 7c, d), their HV and SP components
 366 were markedly different, especially in the Indian Ocean (Fig. 7h, l). The OFES1 and the EN4 showed much the same
 367 global OHC trend (Fig. 7a), but again this was the result of the significant HV and SP components cancelling each
 368 other. The excellent agreement between the EN4 and OFES1 in each basin (Fig. 7b–d) was also the result of
 369 cancellations of notable basin-wide differences, especially in the Pacific and Atlantic Oceans (Fig. 7b, c).

370 To summarize, the OFES2 showed some improvement (better agreement with the EN4) over the OFES1 in the
 371 upper layer (above 300 m), but was more of an outlier in the other two layers. It is essential to examine the HV and
 372 SP when investigating the OHC trends, as different data products may show much the same OHC evolution, but
 373 substantially different HV and SP.



374

375 **Figure 7.** As for Fig. 6 but for the lower layer (700–2000 m).

376 3.2 Temporal evolution of the zonal-averaged potential temperature trend

377 Section 3.1 focused on the temporal characteristics of the global and basin-wide OHC, HV and SP from the three
 378 datasets. Although both similarities and differences were demonstrated, this comparison only in the temporal
 379 domain lacked spatial information. Here, we aim at understanding how the differences were distributed in the
 380 meridional direction. As a first step, we calculated the 10-year rolling trends in the zonal-averaged potential
 381 temperature change for all three datasets (Figs. 8–10). We also calculated the HV and SP components
 382 (Supplementary Information, Figs. 1–6).

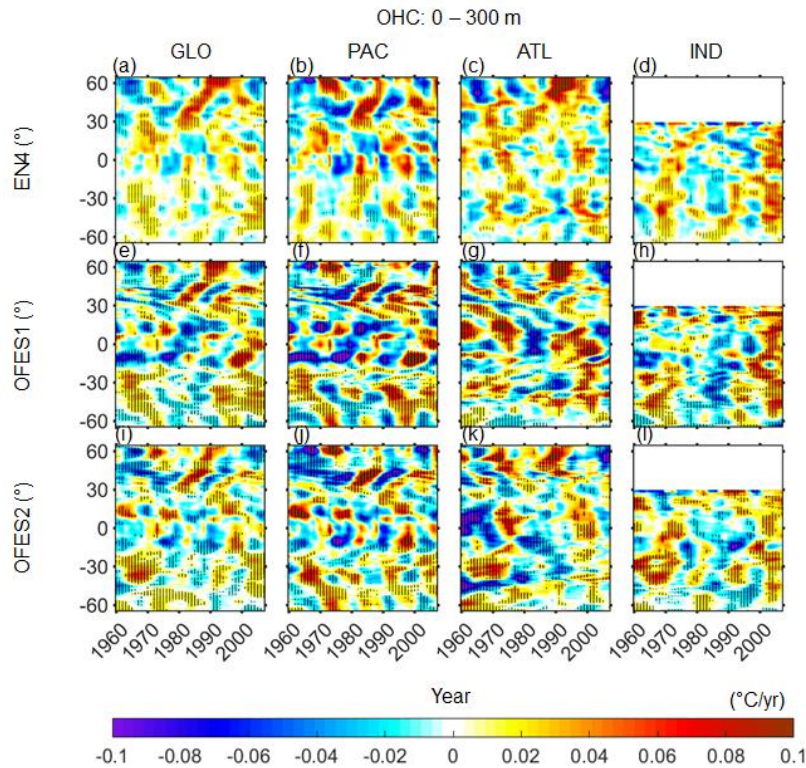
383 The complex patterns shown in Figs. 8–10 defy easy interpretation, so we focus on the large-scale patterns of the
 384 similarities and differences.

385

386 *Upper layer*

387 There was a generally reasonable correlation between these datasets at latitudes 30–60° N for both the Pacific and
 388 Atlantic Oceans (there is no northern high latitude in the Indian Ocean). More specifically, there was a wave-like
 389 cooling trend propagating from around 60° N to 30° N from 1960 to the end of the 1970s in the global ocean; this
 390 apparent propagation was especially clear in the EN4 and OFES2. In addition, there was northward propagation of a
 391 cooling trend in the 1990s between around 30–45° N. It is reasonable to attribute this cooling to the volcanic
 392 eruption of Indonesia’s Mount Agung in 1963, Mexico’s El Chichón in 1982 and the Philippines’ Mount Pinatubo in
 393 1991; the two hindcast simulations were able to reproduce these climate events.

394 Following these cooling events, there were three subsequent warming trends, as the ocean surface temperature
 395 returned back to normal once the aerosols released over several years of volcanic eruptions finally dispersed. Of
 396 these warming trends, that following the El Chichón eruption was the most significant; there was a clear northward
 397 propagation of the warming from around 30° N to the subpolar areas. Interestingly, the contributions to this large-
 398 scale warming and cooling by the SP was comparably to the HV (Supplementary Information, Figs. S1–2),
 399 contradicting the general sense that the HV dominates the potential temperature change. In fact, the above-
 400 mentioned propagation of the cooling patch from around 60 to 30° N in the 1960–70s was, to a larger extent,
 401 associated with the SP.



402 **Figure 8.** Temporal evolution of 10-year rolling trend of the zonal averaged potential temperature change in the upper layer of
 403 the ocean (0–300 m). **Left to right:** global, Pacific, Atlantic and Indian Ocean. **Top to bottom:** EN4, OFES1 and OFES2.
 404 Horizontal axis: year; vertical axis: latitude. Stippling indicates the 95% confidence level. The HV and SP counterparts are in the
 405 Supplementary Information, Figs. S1–6.
 406

407
 408 Equatorward of 30°, large differences emerged in the data. Strong cooling was particularly visible in the OFES1
 409 in the Pacific tropics before around 1990 (Fig. 8f), corresponding to the persistent cooling in the global ocean and
 410 Pacific Ocean from the OFES1 in Fig. 2. In the OFES2 Pacific Ocean, clear differences from the EN4 were discerned
 411 in the low latitudes before around 1980, then a similar pattern to the EN4 was simulated by the OFES2. In the Atlantic
 412 tropics (Fig. 8, 3rd column), there was moderate-to-intense warming in the 1960s in the EN4 and OFES1, but
 413 considerable cooling in the OFES2, which may be a result of poor spun-up in the OFES2. All three datasets captured
 414 the Atlantic tropical warming in the 1970s, and from the 1990s to the 2000s, but the two OFES datasets estimating a
 415 much stronger intensity than the EN4, especially the OFES1. In addition, the OFES1 showed a significant cooling
 416 appearing in the Atlantic tropics in the 1980s (Fig. 8g). Although a similar contemporary cooling was shown by the

417 OFES2, its cooling center was shifted several degrees southward. This 1980s Atlantic tropical cooling was
418 comparatively weak in the EN4. Moreover, the OFES2 indicated an approximate 20-year cooling in the vicinity of
419 45°S in the Atlantic Ocean (Fig. 8k); this cooling in the 1960s existed, but weaker in intensity, in the EN4 and OFES1.
420 In the Indian Ocean, the most significant agreement among the three datasets was the intense warming in the 2000s.
421 In addition, there were some common cooling patterns from the 1980s to the 1990s in all three datasets. Over these
422 latitudes, the HV accounted for more of the potential temperature change than the SP, with the latter in general
423 counteracting the HV (Supplementary Information, Figs. S1–2).

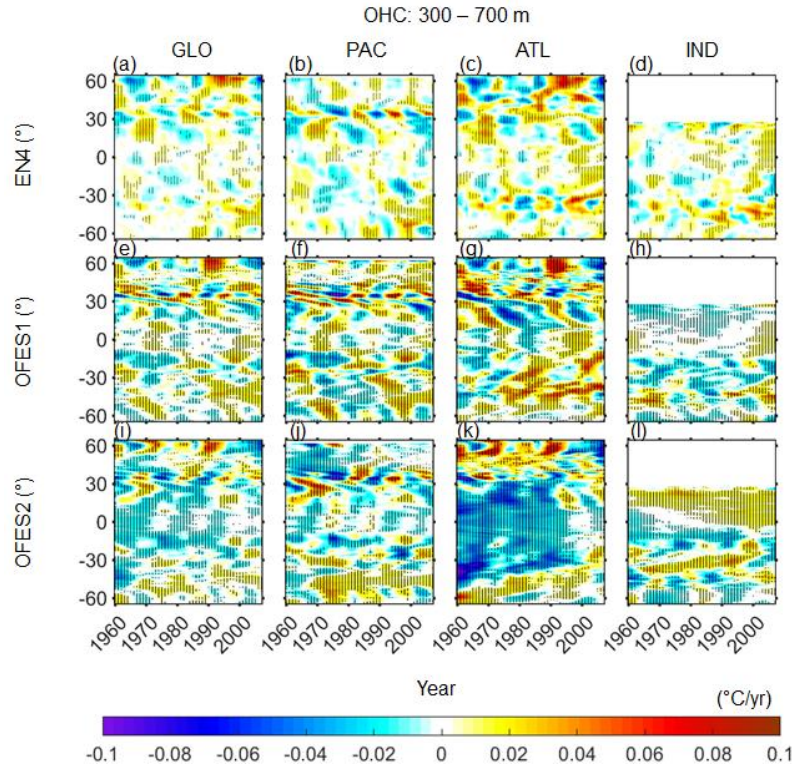
424 A general property of the similarities and differences between these three datasets is that a better agreement was
425 reached in the poleward of 30° than the latitudes equatorward of 30°. A possible explanation for this latitudinal
426 dependence is that a deeper thermocline at a higher latitudes responded less sensitively to the applied wind stress
427 (Kutsuwada et al., 2019). Kutsuwada et al. (2019) found that the NCEP reanalysis wind stress used as the atmospheric
428 forcing of the OFES1 had some issues, causing much shallower thermocline in the tropical North Pacific Ocean and
429 therefore large negative temperature differences when comparing to the observations and an OFES version forced by
430 the wind stress from the satellite measurements (QSCAT). The authors also claimed that the JRA 55 wind stress had
431 similar problems with the NCEP wind. Indeed, the intense Pacific cooling patches in Fig. 2f was likely to be resulting
432 from the abnormally shallower thermocline in the tropical Pacific Ocean, consistent with Kutsuwada et al. (2019),
433 despite different temporal periods were considered.

434

435 *Middle layer*

436 In the middle layer between 0–300 m, the three datasets showed relatively poor agreement compared to the upper
437 layer. The OFES2 differed from the others by showing intense cooling before 2000 in the Atlantic Ocean (Fig. 9k)
438 and moderate but consistent warming in the northern Indian Ocean over most of the whole period (Fig. 9l). In addition,
439 there were large-scale cooling patches in the northern Pacific Ocean and along the Indian Equator from the OFES2,
440 while these cooling were not apparent in the other two datasets. These cooling distributions further showed where and
441 when the cooling trend from the OFES2 in Figs. 3 occurred and can be at least partially attributed to the spin-up issue
442 of the OFES2. However, some similarities between the OFES2 and other two datasets emerged in recent decades. For
443 example, the OFES2 reproduced the marked warming at the high latitudes of the Atlantic Ocean in the 1980s and
444 1990s, and a subsequent cooling (Fig. 9k), similar to the EN4 and OFES1.

445 Comparing the OFES1 with the EN4, both similarities and differences can be discerned. The OFES1 generally
446 agreed with the EN4 north to 30°N, with only a few differences. In the tropics, however, large differences were found
447 between the OFES1 and EN4. For instance, the OFES1 indicated that the northern Indian Ocean was cooling
448 consistently (Fig. 9h), but alternate warming and cooling appeared in the EN4 (Fig. 9d). Furthermore, the intense
449 warming and cooling patches in the southern Atlantic and Indian Oceans, respectively, shown in the OFES1 (Fig. 9g,
450 h), were not clearly visible in the EN4 (Fig. 9c, d). These potential temperature changes mainly resulted from the
451 vertical displacement of the neutral density surfaces, that is, the HV (Supplementary Information, Fig. S3). However,
452 the role of the SP cannot be ignored. This was especially clear in the southern hemisphere in the EN4. The OFES2
453 also showed that the warming of the northern Indian Ocean was largely SP-related.



454
455 **Figure 9.** As for Fig. 8 but for the middle layer (300–700 m).
456

457 *Lower layer*

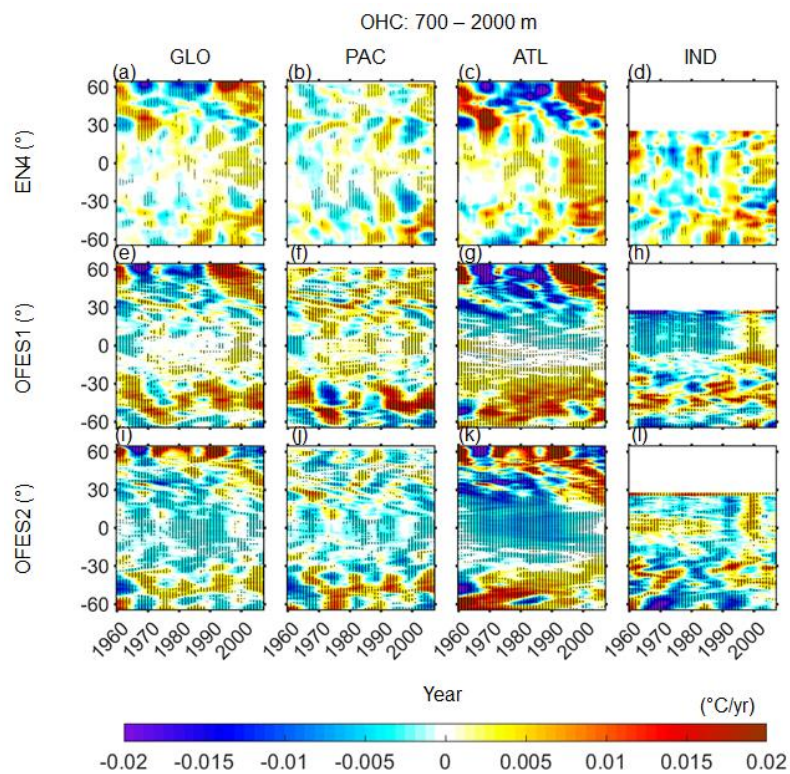
458 The northern Atlantic Ocean, especially north to 30°N, dominated the global potential temperature change in the EN4
459 (Fig. 10); this was related more to the SP, especially in the intense cooling patch (Supplementary Information, Fig.
460 S6). Although the OFES1 agreed well with the EN4 in the northern Atlantic Ocean (> 30° N), there were considerable
461 differences elsewhere between the OFES1 and EN4. More specifically, there was intense HV-associated warming
462 and cooling in the southern Pacific Ocean in the 1960s and 1970s in the OFES1, but not in the EN4 (Supplementary
463 Information, Fig. S5). In addition, the warming of the southern Pacific Ocean since about 1990 was much stronger in
464 the OFES1 than in the EN4. The main reason is that there was strong SP cooling in the southern Pacific Ocean in the
465 EN4 (Supplementary Information, Fig. S6). Moreover, the consistent cooling in the Atlantic tropics, the significant
466 warming in the southern Atlantic Ocean and the intense cooling of the northern Indian Ocean before the middle of the
467 1990s shown by the OFES1 were not evident in the EN4.

468 The OFES2 captured some warming patterns in the southern hemisphere, similar to the OFES; it also agreed with
469 the other two datasets in the intense warming patch in the northern Atlantic Ocean. However, the agreement between
470 the OFES2 and the others was generally poor. Most significantly, cooling was indicated by the OFES2 at the low and
471 middle latitudes in both the Pacific and Atlantic Oceans, especially the latter. Furthermore, both the EN4 and OFES2
472 showed marked but opposite SP variations in the northern Atlantic Ocean north to 30°N, whereas the OFES1 indicated
473 moderate SP in a similar warming/cooling pattern to the EN4.

474 From Fig. 10, it seems that the spin-up may not be the primary reasons for the differences between the two OFES
475 data and the EN4, as there are no clear improvements in the agreements with the EN4 in the recent decades. Another

476 possible is that the two OFES data have not been fully spun-up even after an integration of more than 50 years for the
 477 water in the lower layer.

478 To summarize, the two OFES datasets had come good agreements with the EN4 in the upper ocean layer, but
 479 largely confined to the middle-high latitudes. Poor agreements were found in the ocean beneath. Specifically, in the
 480 middle ocean layer, the OFES1 had a generally reasonable agreement with the EN4, but large differences exist
 481 elsewhere; in the OFES2, intensive cooling patches were simulated, especially in the Atlantic Ocean. Although the
 482 spin-up issue may partially explain the notable differences between the OFES data and EN4 for the ocean below 300
 483 m, other causes responsible for the examined differences are also possible.



484
 485 **Figure 10.** As for Fig. 8 but for the lower layer (700–2000 m). Note the different colour scale.
 486

487 3.3 Depth-time distribution of potential temperature, HV and SP trend

488 Although we divided the top 2000 m into three layers, some detail was lost in taking layer (vertical) averages. In
 489 this section, we compare vertical trends in the potential temperature change ($\Delta\theta_{OHC}$), and its HV ($\Delta\theta_{HV}$) and SP ($\Delta\theta_{SP}$)
 490 components (Figs. 11–13).

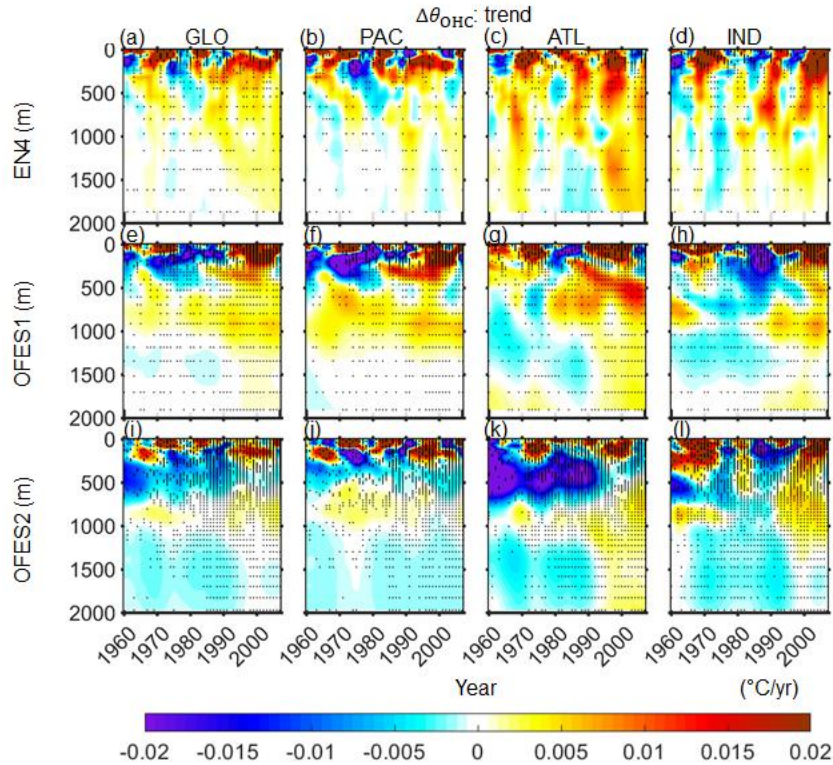
491 For the global ocean, the upper ocean layer above 300 m accounted for most of the warming or cooling (Fig. 11,
 492 left column). The EN4 showed warming over most of the investigated period with a few cooling as a response to the
 493 distinctive climate events. It can be seen that the volcanic eruptions of Mount Agung and El Chichón impacted a
 494 greater depth than the eruption of Pinatubo. The aforementioned strong cooling from the OFES1 in the upper Pacific
 495 layer before 1990 started at a greater depth in the beginning and subsequently ending at a shallower depth (Fig. 11e).
 496 At greater depths, moderate warming or cooling can be found. Specifically, in the EN4, moderate warming can be
 497 seen far deep to around 2000 m since around the early 1990s. The OFES1 showed moderate warming between 500–

498 1000 m over almost the whole investigated period. Since around the middle of 1990s, a weak warming extended to
499 the 2000 m based on the OFES1. The differences of the OFES2 from the other two datasets are apparent in the global
500 ocean below around 200 m, where cooling is the dominant pattern except some weak warming patches between 500–
501 1000 m (Fig. 11i).

502 In the Pacific Ocean, the OFES2 had a generally reasonable agreement with the EN4 above around 200 m, whereas
503 the agreement between the OFES1 and the EN4 was poor, despite of some similar warming or cooling patches. Further
504 below, the EN4 showed periodic warming and cooling. The OFES1 showed consistent warming between around 500–
505 1200 m, whereas the OFES2 estimated consistent cooling with some exceptions between 500–1000 m. Although
506 beyond the scope of this work, the question on why both the OFES1 and OFES2 showed relatively consistent warming
507 between 500–1000 m, around the depth of the permanent thermocline, necessitate a further work.

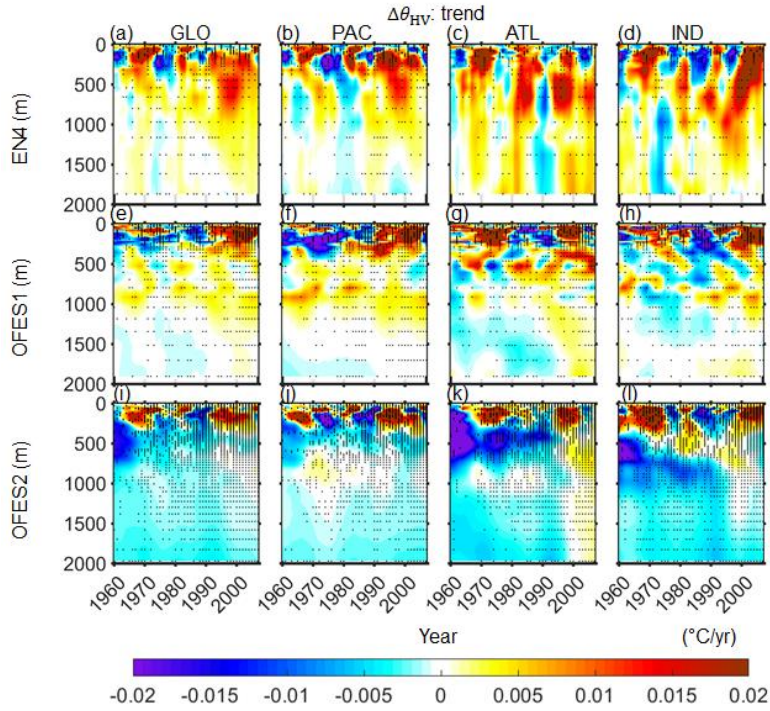
508 In the Atlantic Ocean, intense warming or cooling extended deeper when compared to the Pacific Ocean.
509 Specifically, the strong warming in the 1980–90s from the EN4 appeared as deep as around 750 m and moderate
510 warming extended to 2000 m since the middle of 1990s. The OFES1 well captured the warming in the 1970s and
511 1990s, and a subsequent cooling in the 2000s, in the upper layer of the Atlantic Ocean when compared to the EN4.
512 However, the OFES1 estimated a strong cooling in the 1980s in the upper layer of the Atlantic Ocean, which was
513 invisible in the EN4. Interestingly, the OFES1 showed a downward propagation of a strong warming from around 200
514 m to around 800 m since the early 1980s; a downward propagation of cooling from around 600 m to 1800 m can also
515 be seen in the OFES1 Atlantic Ocean (Fig. 11g). Similar to the EN4, moderate warming extended to 2000 m since
516 around the middle of 1990s. As for the OFES2, the most prominent pattern distinguishing it from the others are the
517 extensive cooling patch before around 1990. In addition, it showed moderate cooling below 1000 m before around
518 1990. These two extensive cooling patterns in the upper-middle and deep layers of the Atlantic Ocean by the OFES2
519 raised questions: what are the main causes of these two cooling patches in the OFES2 and why they suddenly stopped
520 at around 1990. One possible reason is that improvement of the reanalysis product of the atmospheric forcing since
521 1990, especially the surface heat flux and wind stress, the latter of which has been shown to be essential to the
522 subsurface temperature simulations ([Kutsuwada et al. 2019](#)).

523 In the Indian Ocean, both the OFES1 and OFES2 captured the warming in the 1960–70s and in the 2000s. However,
524 the OFES1 presented an intense cooling in the upper layer in the 1980s; a similar but less extensive cooling can also
525 be seen in the OFES2. Below the upper layer, the EN4 showed largely warming with a major exception of cooling in
526 the 1970s. The two OFES presented notably different patterns. Specifically, between 500–1000 m, there were
527 moderate warming with an intermittent in both the OFES datasets. The intermittent appeared later in the OFES2
528 compared to the OFES1. Below 1000 m, moderate cooling dominated before the middle of 1990s, as shown in both
529 the OFES datasets.



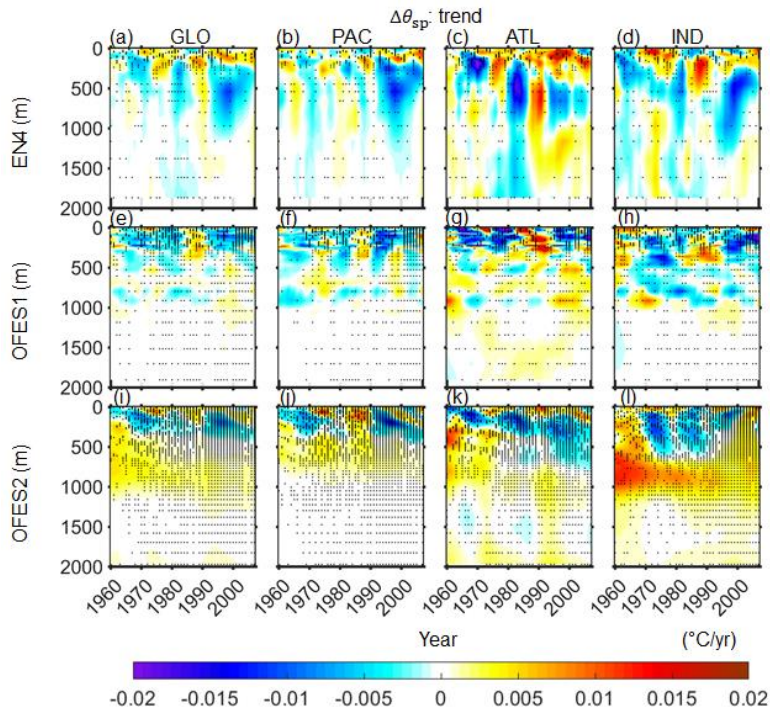
530
 531 **Figure 11.** Depth-time patterns of the horizontally averaged potential temperature change $\Delta\theta_{\text{OHC}}$ for (left to right) the global,
 532 Pacific, Atlantic and Indian Oceans. **Top to bottom:** EN4, OFES1 and OFES2. Horizontal axis: year; vertical axis: depth in m.
 533

534 To a great extent, the HV components dominated the OHC variations by comparing the Fig. 12 with Fig. 11. For
 535 instance, the profound warming and cooling patterns in Fig. 11 were mostly associated with the HV component. Also,
 536 the moderate cooling below 1000 m in the OFES2 was also mainly related to the HV. Although the SP was generally
 537 weaker and less important than the HV in accounting for the OHC variations, its role cannot be ignored. Indeed,
 538 intense SP-associated warming or cooling were presented in the EN4 in all the major basins. The increased subsurface
 539 SP cooling since 1990s in the Pacific and Indian Oceans were particularly interesting. One speculation is that this may
 540 be related to the great increase of the subsurface salinity observations since 1990s. A possible explanation for the
 541 appearance of the prominent SP cooling in the Pacific and Indian Oceans, but not in the Atlantic Ocean is that the
 542 Atlantic Ocean has been better observed than the Pacific and Indian Oceans before 1990s. Another interesting point
 543 with regards to the SP is the consistent SP warming in the OFES2, but not visible in the other two datasets.



544

545 **Figure 12.** Depth-time patterns of the horizontally averaged potential temperature change from the HV component, $\Delta\theta_{HV}$, for
 546 (left to right) the global, Pacific, Atlantic and Indian Oceans. **Top to bottom:** EN4, OFES1 and OFES2. Horizontal axis: year;
 547 vertical axis: depth in m.



548

549 **Figure 13.** Depth-time pattern of the horizontally averaged potential temperature change from the SP component, $\Delta\theta_{SP}$, for (left to
 550 right) the global, Pacific, Atlantic and Indian Oceans. **Top to bottom:** EN4, OFES1 and OFES2. Horizontal axis: year; vertical
 551 axis: depth in m.

552

553 **3.3 Spatial patterns of the potential temperature, HV and SP trends**

554 To gain a more detailed understanding of the similarities and differences between the potential temperature trends
555 from the three datasets, we presented the spatial distributions of the potential temperature change ($\Delta\theta_{OHC}$), and its HV
556 ($\Delta\theta_{HV}$) and SP ($\Delta\theta_{SP}$) components in the three ocean layers (Figs. 14–16).

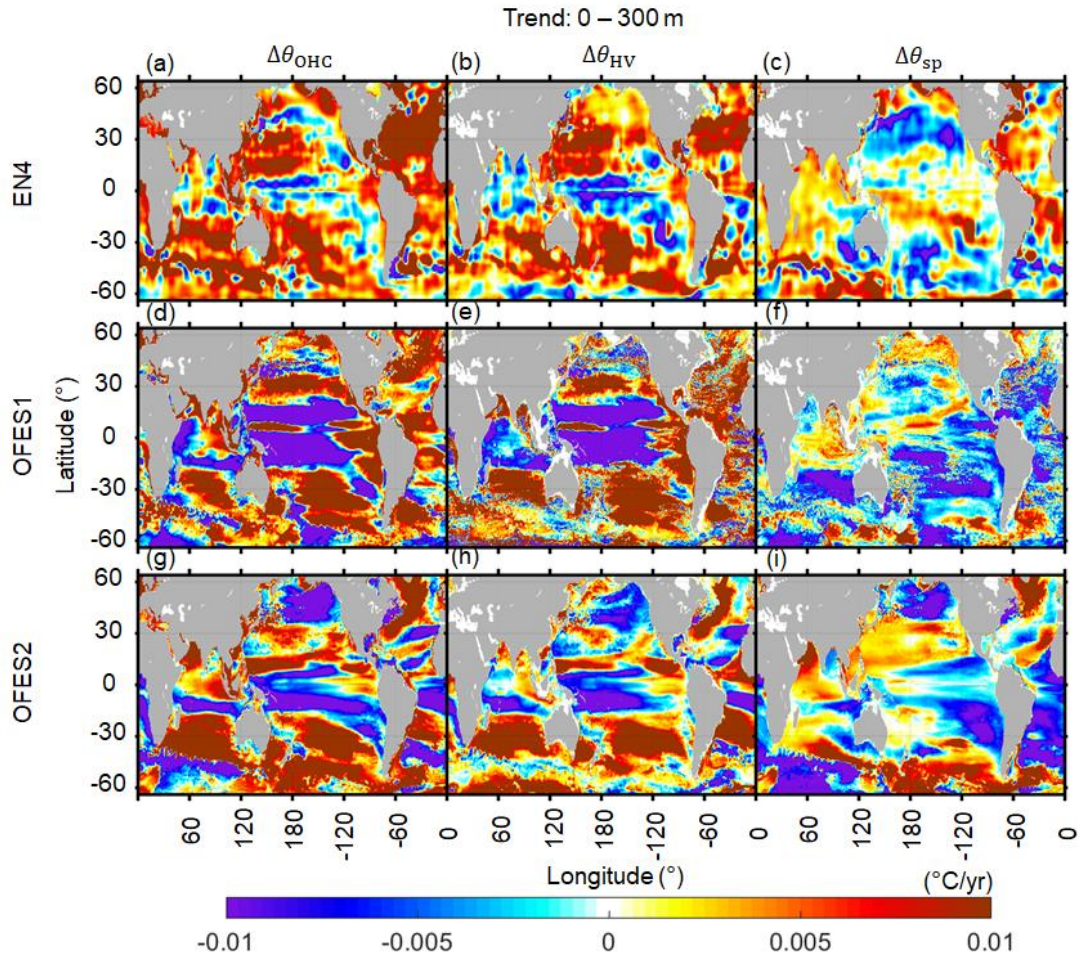
557

558 *Upper layer*

559 Warming was almost ubiquitous in the EN4 (Fig. 14a), particularly strong in the northern Atlantic Ocean and in the
560 Southern Ocean. These two hotspots of warming were expected from both theories and models. Specifically, the
561 shallow ocean ventilation in these two regions could warm faster than the global average (Banks and Gregory 2006;
562 Durack et al. 2014; Fyfe 2006; Talley 2003). Major exceptions of cooling appeared in the Eastern Pacific Equator,
563 along the north Pacific Current, in a meridional band in the southeastern Pacific Ocean, in part of the Argentine Basin
564 and in the southern Indian tropics. All of these cooling regions consists of a small fraction of the global ocean. As
565 with the EN4, both the OFES datasets showed significant warming in the subtropics, high-latitude of the northern
566 Atlantic Ocean and in the Arabian Sea in the Indian Ocean. In addition, the OFES1 was similar to the EN4 in showing
567 cooling along the north Pacific Current. Despite of these similarities, large differences exist between these three
568 datasets. The most significant difference was in the Pacific tropics. Although, as noted earlier, there was a zonal band
569 of cooling in the Pacific tropics in the EN4, this zonal band in the OFES1 and OFES2 was much stronger in intensity
570 and more extensive and mainly related to the HV, especially in the OFES1. These abnormally stronger cooling pattern
571 in the vicinity of Equator were likely to be resulting from the poor qualities of the atmospheric wind stress over some
572 periods. As mentioned earlier, Kutsuwada et al. (2019) demonstrated that the NCEP wind stress used as the forcing
573 of the OFES1 cause much shallower thermocline in the north Pacific tropical area and therefore significant negative
574 differences relative to the observations. In the northeast of the Pacific Ocean, the OFES2 but not the OFES1 and EN4,
575 showed a patch of intense cooling, corresponding to the cooling pattern in the 1960–70s (Fig. 8j). the OFES2 also
576 showed four large cooling areas in the Atlantic Ocean (Fig. 14g). In the Indian Ocean, unlike the EN4, there was a
577 patch of intense cooling along the western coast and in the Indian sector of the Southern Ocean from the OFES1 and
578 OFES2, respectively.

579 The decomposition of the potential temperature changes into HV and SP components showed that the EN4 warming
580 was largely the result of isopycnal deepening (HV) in the subtropics. This is consistent with the finding that the
581 subtropical mode water (STMW) is the primary water mass accounting for global warming (Hakkinen et al., 2016),
582 as we also show later. The SP was generally weaker than the HV, and tended to counteract the HV warming, especially
583 in the subtropics. This dampening effect can be easily understood from Fig. 1 of Hakkinen et al. (2016). For example,
584 in a stratified ocean with warm/salty water above cold/fresh water, typical of the subtropics, a pure warming of one
585 water parcel can be considered as a sum of warming and salination along its original potential-temperature/salinity
586 characteristic (HV part), and a cooling and freshening along the new isopycnal (SP). Two major exceptions were the
587 northern Atlantic subtropics and the Indian Ocean, where SP was mostly warming. The SP warming in the northern
588 Atlantic subtropics results from a large salinity increase through evaporation (Curry et al., 2003; Hakkinen et al.,
589 2016). Similarly, we found that positive SP warming also occurred in most of Indian Ocean, except west to the

590 southwest Australia. Indeed, this SP-related warming in the northern Indian Ocean dominated the potential
 591 temperature change, especially in the Arabian Sea. The most significant SP warming, however, was found in the
 592 Indian sector of the Southern Ocean (may be related to the freshening of the Southern Ocean), in the southern
 593 subtropics of the Atlantic Ocean and in the Labrador Sea (Fig. 14c).



594
 595 **Figure 14.** Spatial distributions of $\Delta\theta_{\text{OHC}}$ (top row), $\Delta\theta_{\text{HV}}$ (middle row) and $\Delta\theta_{\text{SP}}$ (bottom row), 1960–2016, in the top ocean
 596 layer (0–300 m). Left to right: EN4, OFES1 and OFES2. Standard deviations of $\Delta\theta_{\text{OHC}}$, $\Delta\theta_{\text{HV}}$ and $\Delta\theta_{\text{SP}}$ are given in the
 597 Supplementary Information.
 598

599 Comparing the HV components in the three datasets showed that the two OFES simulations were able to reproduce
 600 the subtropical HV warming pattern, although less accurately in the northern Pacific subtropics. The strong and
 601 extensive equatorial cooling in the Pacific and Indian Oceans was largely associated with the HV in the two OFES
 602 datasets.

603 The SP in the OFES1 was similar to the EN4 in the northern subpolar region of the Pacific Ocean, in part of the
 604 northern Pacific subtropics, in the Labrador Sea and in part of the northern Indian Ocean. The OFES2 SP was similar
 605 to the EN4 in the Labrador Sea and the western Indian Ocean. In general, however, there were no common patterns
 606 in most of the global ocean. In particular, neither of the OFES datasets captured the SP warming in the northern
 607 Atlantic subtropics, and the OFES2 indicated moderate SP warming in the north Pacific subtropics and intense SP

608 warming in the Pacific sector of the Southern Ocean, respectively. The improvements of SP from the OFES1 over that
609 from the OFES1 in the Arabian and Indonesian Seas but not in the Bengal Bay was consistent with the S2020, to some
610 extent. The authors demonstrated smaller bias in the water properties in the Arabian and Indonesian Seas, but large
611 salty bias remained in the Bengal Bay in the OFES2.

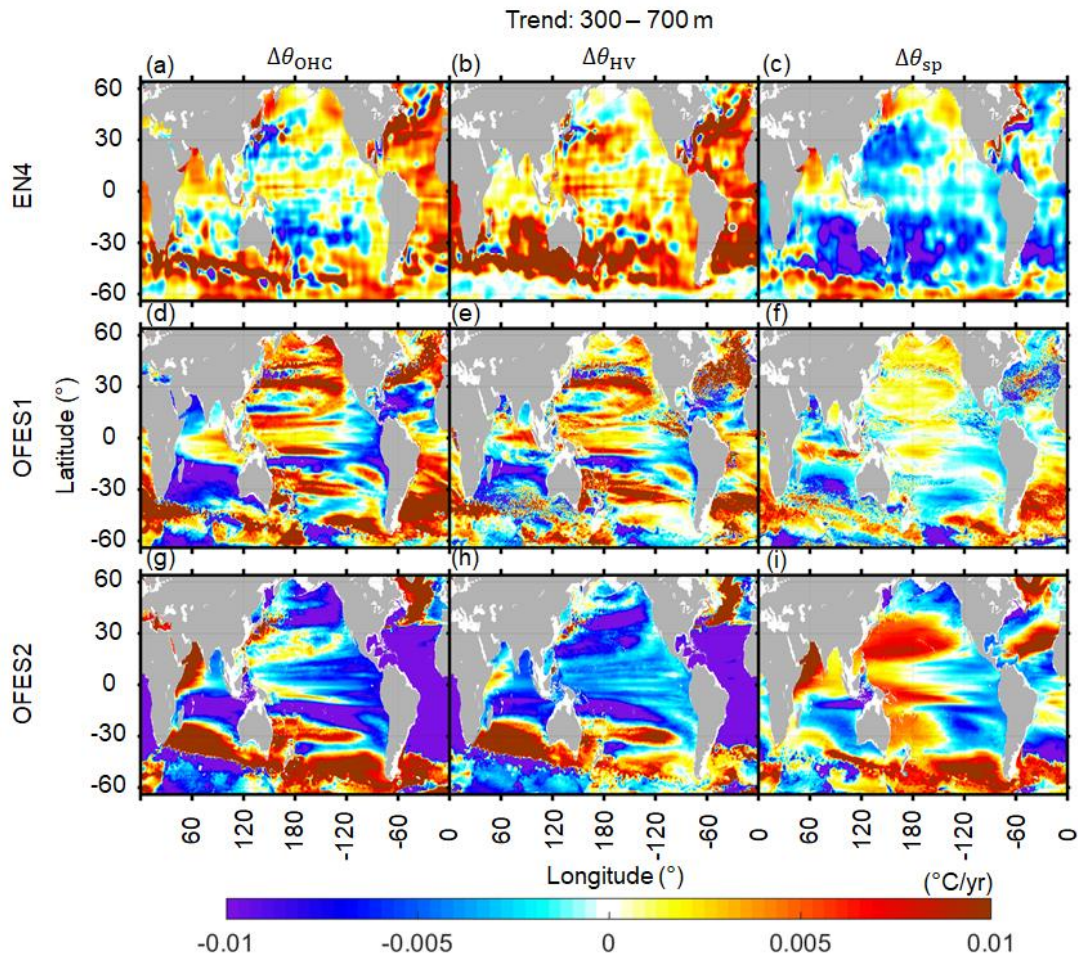
612 In Fig. 3, we showed that the SP was highly similar between the EN4 and OFES2 in the upper layer of the Pacific
613 Ocean. However, the spatial distributions of the SP component in the Pacific Ocean were seldomly similar between
614 the EN4 and OFES2. That is, the time series of a basin-wide quantity hides many details.

615 616 *Middle layer*

617 The EN4 showed cooling in the ocean, concentrated in the southern Pacific subtropics and in the region associated
618 with the Kuroshio (Fig. 15a). For the rest of the global ocean, especially over the bulk of the Atlantic Ocean, in the
619 northern Indian Ocean and along the ACC path in the Southern Ocean, clear warming was presented, accompanied by
620 sporadic cooling patches. The OFES1 could reproduce some warming patterns in the northern Pacific Ocean, the bulk
621 of the Atlantic Ocean, in the eastern part of the northern Indian Ocean and parts of the ACC path. However, notable
622 differences can be found between the OFES1 and EN4. Among these differences, the most prominent is the intense
623 cooling in the southern Indian Ocean from the OFES1, which was found to occur in the 1990s from Fig. 3(d). In
624 addition, strong cooling patches were also found in the southern Pacific tropics, west to the central-south America in
625 the northern Atlantic subtropics, in the Arabian Sea and along the part of southern edge of the ACC. The pattern in
626 the OFES1 Pacific Ocean clearly appears as zonal bands, but this zonality property was obscure in the EN4. Consistent
627 with Fig. 3, intense cooling was simulated in all the major basins, with most prominent in the Atlantic Ocean. Besides
628 these notable cooling patches, large-scale strong warming patterns were found in the Kuroshio region, in the southern
629 Pacific and Indian subtropics, in the northern Atlantic Ocean (north to 35° N), in the western part of the northern
630 Indian Ocean and in the Pacific and Atlantic sectors of the Southern Ocean. In general, over the bulk of the global
631 ocean, there were apparent differences between these three datasets. The above 700 m was relatively well observed,
632 especially in the Atlantic Ocean (even back to 1950–60s, Hakkinen et al., 2016). Therefore, it is likely that the OFES2
633 was the outlier at this multi-decadal scale and there were some potential problems in the OFES1, for example, in the
634 southern Indian Ocean.

635 Interestingly, the HV warming was almost ubiquitous in the middle layer from the EN4, especially in the Southern
636 Hemisphere, consistent with the warming shift towards to the Southern Hemisphere found in Hakkinen et al. (2016).
637 Correspondingly, the SP cooling also occupies most of the global ocean, with a similar southern shift, most prominent
638 to the east and west of the Australia. The major SP warming patches were found in the Sea of Okhotsk, north to the
639 Gulf Stream, in the Arabian Sea and along the southern edge of the ACC. These regions are generally associated with
640 strong salinity variations. Comparing the HV and SP between the EN4 and OFES1 showed that the OFES1 captured
641 some warming patterns in the Pacific and Atlantic, but not the Indian, subtropics. The HV agreement in the southern
642 Pacific and Indian tropics and in the Southern Ocean were mostly poor. As for the SP, the OFES1 reproduced the
643 intense SP cooling west to the Australia and in the southern Pacific subtropics, despite of smaller coverage compared
644 to the EN4. However, the OFES1 showed almost opposite SP trends over most of the global ocean. In the OFES2,
645 both the HV and SP were strong, but the basin-wide cooling was mainly the result of HV. Overall, the OFES2 had a

646 reasonable agreement with the EN4 in the southern subtropics in terms of HV. It also had a common HV warming
 647 patch in the northern Atlantic Ocean (north to 35° N) as the EN4. With regards to the SP, the OFES2 was similar to
 648 the EN4 in showing SP warming in the Arabian Sea and parts of the southern edge of the ACC. Also, it captured the
 649 SP cooling in the eastern Pacific Ocean, along the Gulf Stream path, west to the Australia. Except of these similarities,
 650 however, the OFES2 was generally opposite to the EN4.

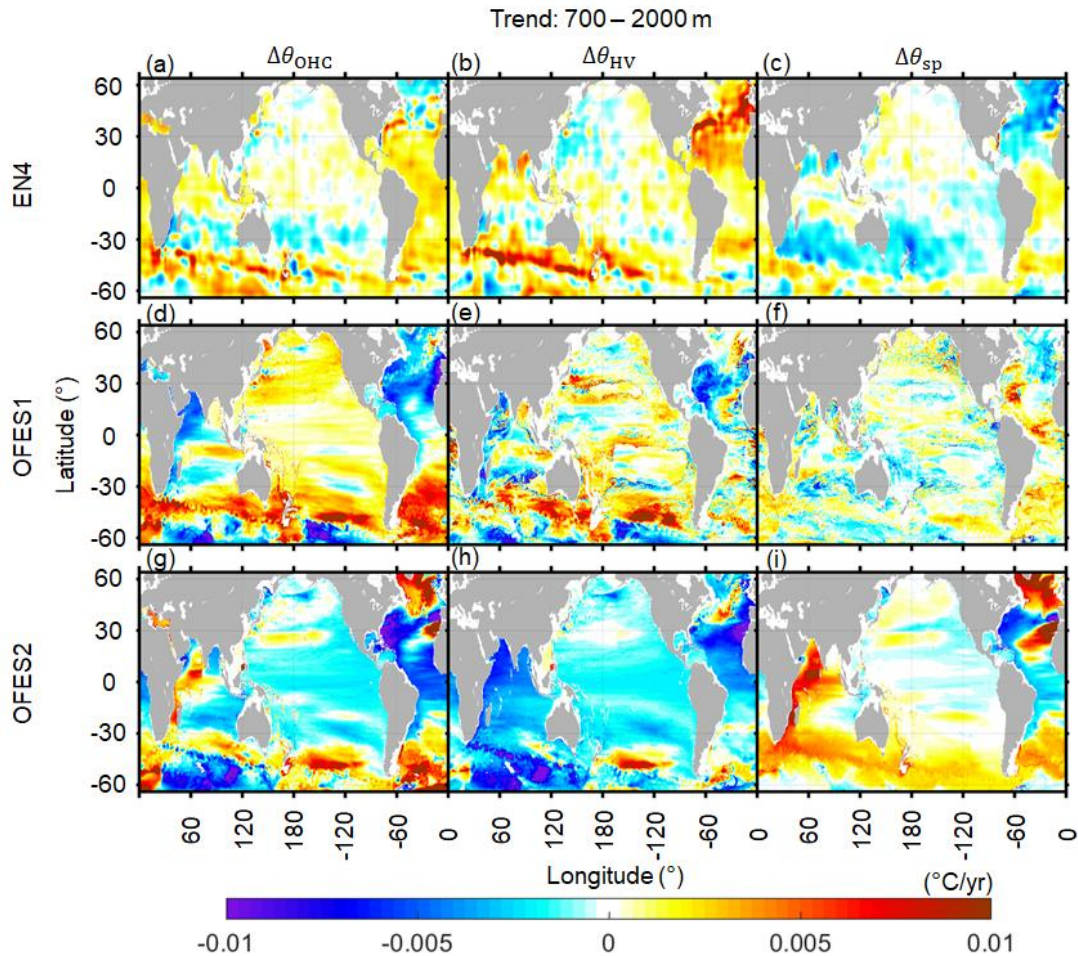


651
 652 **Figure 15.** As for Fig. 14 but for the middle layer (300–700 m).
 653

654 *Lower layer*

655 The warming and cooling intensities were generally much weaker than in the top two layers, consistent with many
 656 previous findings that more ocean heating occurs in the upper 700 m than at greater depths (Hakkinen et al., 2016;
 657 Levitus et al., 2012; Wang et al., 2018; Zanna et al., 2019). The EN4 showed widespread warming patches in the
 658 Southern and Atlantic Oceans, as well as three large zonal bands of cooling in the southern subtropics of the Pacific
 659 and Indian Oceans, and in the northern subpolar region of the Atlantic Ocean (Fig. 16a). Similar to the EN4, warming
 660 was seen along the northern edge of the ACC and in the southern Atlantic Ocean in the OFES1, but with much stronger
 661 intensity than the EN4 (Figs. 16a, d). There was also moderate warming over almost the whole Pacific Ocean in the
 662 OFES1. Significant differences between the OFES1 and EN4 were found in the northern Atlantic Ocean, where the
 663 OFES1 showed extensive cooling compared to the moderate warming in the EN4. There was also strong cooling in

664 the OFES1 Arabian Sea, in contrast to the quite weak warming in the EN4 Arabian Sea. To some extent, the OFES2
 665 was similar to the other two in showing warming along the northern edge of the ACC and in the southern Atlantic
 666 Ocean south to 30°S (Fig. 15g), despite of the intensity differences. It also showed cooling in the low and middle
 667 latitudes of the Atlantic Ocean, as did the OFES1 but opposite to the EN4. However, the bulk of the Pacific Ocean
 668 was shown to be cooling in the OFES2, which was almost opposite to the OFES1 (Fig. 15d) and only similar to the
 669 EN4 in part of the southern Pacific subtropics (Fig. 15a). Moreover, intense and widespread cooling appeared in the
 670 Indian sector of the Southern Ocean in the OFES2. The warming of the northern ACC was captured by the OFES2.



671
 672 **Figure 16.** As for Fig. 14 but for the lower layer (700–2000 m).
 673

674 In the EN4, there was intense HV warming along the northern edge of the ACC in the Indian and Pacific Oceans,
 675 and in the northern Atlantic Ocean (Fig. 16b), which largely accounted for the total potential temperature variations
 676 and were generally accompanied by SP cooling (Fig. 16c). In the northern Atlantic tropics and southern Atlantic
 677 Ocean, moderate HV and SP warming coexist. We found that the OFES2 captured the HV warming pattern along the
 678 northern edge of the ACC, being consistent with the EN4. However, there were remarkable differences from the EN4,
 679 particularly in the northern Atlantic and Indian Oceans. As for the SP, there were some similarities between the OFES1
 680 and EN4, for example, they both had SP cooling and warming in the northern and southern Atlantic Ocean,
 681 respectively. Among the three datasets, the OFES2 showed the most extensive and strong but generally cooling in the

682 HV component, except a patch of HV warming in the Pacific sector of the Southern Ocean, and such a warming patch
683 was also seen in the EN4. In contrast, intense SP warming was estimated in the OFES2 in the Southern Ocean, in the
684 western Indian Ocean, in the northern Atlantic subpolar regions and a large-scale patch of abnormally strong SP
685 warming associated with the Mediterranean Overflow Water (MOW). This very strong SP warming related to the
686 MOW is likely the result of the unrealistic spreading of salty Mediterranean overflow found in S2020.

687 Besides the above-discussed multi-decadal linear trend, we have demonstrated that (not shown here) the significant
688 differences between the two OFES datasets and the EN4 were much reduced if we considered only the period between
689 2005–2016, which was argued to be well spun-up by S2020. In addition, over this 12-year period, the spatial pattern
690 of the OFES2 did show some improvements over the OFES1 for upper and middle layers, but not necessarily for the
691 lower layer, when taking the EN4 as a reference. Does this better agreement come from a better spun-up or come from
692 the improvements of the reanalysis product of the atmospheric forcing for these two OFES data? This interesting
693 question would require a further detailed exploration in the future.

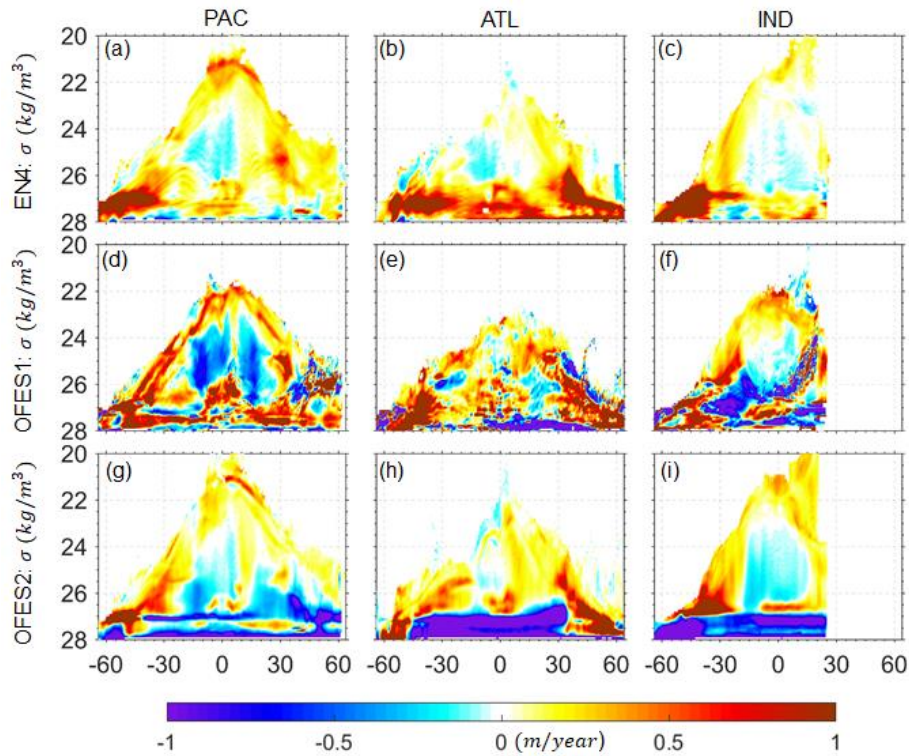
694 **3.4 Trends in the HV and SP in the neutral density domain**

695 To analyse the warming and cooling from the perspective of water mass, it is useful to show the HV and SP
696 components in neutral density coordinates, as suggested by one reviewer. Following [Hakkinen et al. \(2016\)](#), we
697 calculated the linear trend (over 1960–2016) in the zonal-averaged sinking of the neutral density surfaces in each
698 major basin (Fig. 17) and the SP-related warming or cooling along the neutral density surfaces (Fig. 18).

699 Our results based on the EN4 were similar to those of [Hakkinen et al. \(2016\)](#), using the EN4, although they used
700 an earlier EN4 version (EN4.0.2) and considered the period over 1957–2011. Specifically, our EN4 results similarly
701 showed that the bulk of HV warming (deepening of neutral density surfaces) was associated with a water mass of over
702 26 kg/m^3 , and mainly concentrated south to 30° S , to wit, from the ventilation region at high latitudes to the subtropics.
703 There was one exception in the Atlantic Ocean, where warming also occurred at the low-middle latitudes and in the
704 northern Atlantic Ocean. The concentrated warming in the northern Atlantic Ocean was attributed to the phase change
705 of North Atlantic Oscillation (NAO) from negative in the 1950–60s to positive in the 1990s ([Hakkinen et al. 2016](#);
706 [Williams et al. 2014](#)). As explained in [Hakkinen et al. \(2016\)](#), these significant deepening of neutral density surfaces
707 were associated with the Subtropical Mode Water (STMW, $26.0 < \sigma_0 \text{ (kg/m}^3) < 27.0$) and the Subantarctic Mode
708 Water (SAMW, $26.0 < \sigma_0 \text{ (kg/m}^3) < 27.1$). These vertical displacements of neutral density surfaces may have resulted
709 from heat uptake via subduction, which then spread from these high-latitude ventilation regions. The large vertical
710 deepening of the STMW and SAMW would then push the Subpolar Mode Water (SPMW, $27.0 < \sigma_0 \text{ (kg/m}^3) < 27.6$)
711 and Antarctic Intermediate Waters (AAIW, $27.1 < \sigma_0 \text{ (kg/m}^3) < 27.6$) down. However, as the vertical displacement of
712 the STMW/SAMW was larger, its volume would have therefore increased and the volume of the underlying
713 SPMW/AAIW decreased ([Hakkinen et al., 2016](#)). Besides these significant sinking of neutral density surfaces, there
714 was generally a shoaling pattern of lower density ($\sigma_0 \text{ (kg/m}^3)$) ranging from 24–26, and mainly concentrated between
715 the Equator and 30° S . To a large extent, this shoaling occurred in the central water, for example, the South Pacific
716 Central Water (SPCW).

717 Here, our focus is not on the detailed mechanisms of warming from the perspective of water mass, as it was in
 718 previous studies. Instead, we focus on the differences between the datasets in the trends of the HV and SP.

719 It can be seen that along the surfaces of the Pacific and Indian Oceans, there was generally an appearance of HV
 720 warming in almost all the three datasets. In the Atlantic Ocean, however, the EN4 estimated a sea surface cooling
 721 south to 30° S and in the northern tropics; the OFES2 also estimated a cooling trend in the Atlantic tropics. Different
 722 from both the EN4 and OFES2, the OFES1 showed an intense cooling pattern along the Atlantic surface between
 723 around 30–50° N.



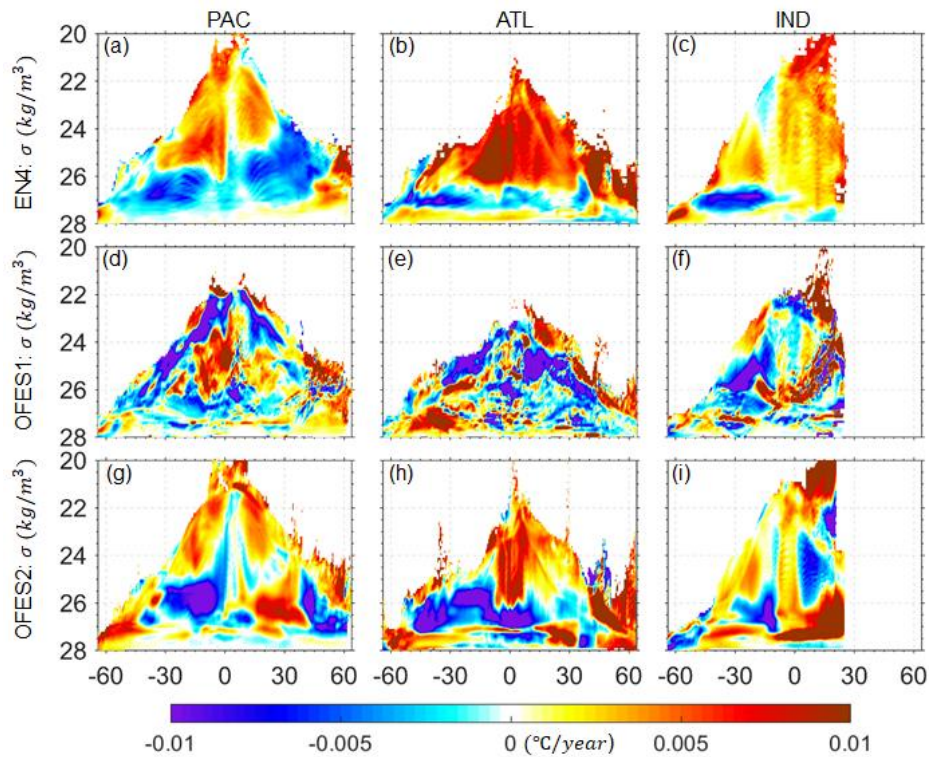
724
 725 **Figure 17.** Linear trends in the zonal-averaged sinking of the neutral density surfaces in the Pacific (**left column**), Atlantic (**middle**
 726 **column**) and Indian (**right column**) Oceans. **Top to bottom:** EN4, OFES1, OFES2. Positive values mean deepening of the neutral
 727 density surfaces. The calculation was for the water above 2000 m.
 728

729 South to 30° S, large downward movements associated with the STMW, SAMW and AAIW were found in all the
 730 three basins in the EN4; in the OFES1, the dominant pattern in the three basins was sinking but was surrounded by
 731 shoaling patches; larger differences from the EN4 were found in the OFES2, which showed significant and extensive
 732 shoaling patterns, especially in the Indian Ocean. The almost opposite trend in the vertical displacements of the neutral
 733 density surfaces between the OFES2 and the observational-based EN4 may indicate that the water mass properties
 734 simulated in the OFES2 were unrealistic, at least at this multi-decadal scale.

735 In the ocean interior between 30°S and 30° N, the OFES1 presented shoaling patterns in the northern and southern
 736 Pacific and Indian Oceans, but not prominent in the Atlantic Ocean. Although these shoaling patterns in the Pacific
 737 and Indian Oceans were also seen in the EN4, as noted earlier, the magnitude in the EN4 was generally much smaller.
 738 The OFES2 had a better agreement with the EN4 in the shoaling pattern in the southern Pacific subtropics. It also

739 captured the shoaling in the EN4 Indian Ocean, with a similar coverage but generally stronger. The shoaling in the
 740 southern Atlantic subtropics was not typical in the OFES2, similar to the OFES1 but different from the EN4.

741 North to 30° N, sinking was widespread in the EN4, particularly strong in the northern Atlantic Ocean. This very
 742 strong sinking in the northern Atlantic Ocean came mainly from the SPMW and STMW. In the EN4 Pacific Ocean,
 743 there was some shoaling patches, which was related to the North Pacific Intermediate Water (NPIW), and to a large
 744 extent, corresponded to the HV cooling in Fig. 16(b). In the OFES1, the pattern was filled with both sinking and
 745 shoaling patches and defies easy interpretation. However, an apparent outlier is the intense shoaling in the OFES1
 746 northern Atlantic Ocean (mainly below 700 m from Figs. 14–16), just opposite to the EN4. The shoaling of neutral
 747 density surfaces in the OFES2 Pacific Ocean north to 30° N was even more prominent than in the OFES1. The OFES2
 748 had a better agreement with the EN4 in the sinking patterns in the Atlantic Ocean north to 30° N.



749 **Figure 18.** Linear trends in the zonal-averaged warming or cooling along the neutral density surfaces in the Pacific (**left column**),
 750 Atlantic (**middle column**) and Indian (**right column**) Oceans. **Top to bottom:** EN4, OFES1, OFES2.
 752

753 The major SP warming in the EN4 Pacific Ocean was associated with the STUW and Pacific Central Water in the
 754 low and middle latitudes, with a shift towards to the southern hemisphere. The northern high-latitude SP warming was
 755 mainly related to the Pacific Subarctic Intermediate Water (PSIW). The two SP cooling came from the STMW,
 756 corresponding to the sinking pattern in Fig. 17(a). This HV warming / SP cooling was particularly typical in the
 757 subtropical regions and the HV warming / SP warming was typical in the subpolar regions, as noted above and more
 758 details were presented in [Hakkinen et al. \(2016\)](#). Very strong SP warming occurred in the Atlantic Ocean, resulting
 759 from salination via the evaporation process. In the southern Atlantic Ocean, pattern of SP cooling is mostly associated
 760 with the sinking of STMW.

761 The SP pattern from the OFES1 was quite noisy and had generally poor agreements between the OFES1 and the
762 EN4 in terms of SP warming, which is likely to be resulting from some issues of salinity simulation in the OFES1. As
763 shown in S2020, the OFES1 was not capable of simulating salty outflows, for example, the outflow through the Persian
764 Gulf into the Indian Ocean. There were notable improvements in the salinity field in the OFES2 over OFES1, mainly
765 attributed to the inclusion of river runoff and a sea-ice model, but some issues still remained, e.g., poor performance
766 in the simulation the Mediterranean outflow. Overall, the SP warming pattern in the density coordinate was
767 significantly improved in the OFES2 when compared to the OFES1. When combing Figs. 14–16, however, one can
768 see that the similarities in the SP estimation between the OFES2 and the EN4 was confined to small fraction of the
769 global ocean, mainly in the upper and middle layers of the Labrador Sea and the northern Indian Ocean in the Southern
770 Ocean. In addition, the OFES2 was also similar to the EN4 in showing a patch of SP cooling in the western part of the
771 northern Atlantic subtropics.

772

773 **3.5 A basin-wide heat budget analysis**

774 The fundamental mechanisms controlling the oceanic thermal state include the net surface heat flux, the zonal and
775 meridional heat advection in the horizontal direction and the vertical heat advection and diffusion (Fig. 1b). Lateral
776 heat diffusion was not considered here, as it was found to play a minor role from our analysis (not shown). Since our
777 focus is on the global and basin-wide OHC in the three vertical layers, we calculated and compared the inter-basin
778 heat exchange, and the vertical heat advection and diffusion, integrated over each basin from 1960–2016. No vertical
779 heat diffusivity data were available from the OFES1, and the vertical heat diffusivity from the OFES2 was temporarily
780 unavailable due to a security incident. This prevented us from calculating the vertical heat diffusion directly. As an
781 alternative, we calculated the residual of the OHC change and all the related heat transport into each basin, and took
782 it as a proxy for the vertical diffusion. This indirect method may suffer from some errors, for instance, it includes the
783 impacts of river runoff in the OFES2, but can still provide us with important information. Our calculations are listed
784 in Tabs. 2–4. The related time series of these surface heat flux and heat advection were shown in the supplementary
785 Figs. S7–9.

786

787 *Upper layer*

788 In the Pacific Ocean, the changing rate of the time-averaged OHC was rather low in both the OFES1 and OFES2.
789 However, the averaged surface heat flux in the OFES1 was twice that in the OFES2, indicating that more heat was
790 injected to the OFES1 Pacific Ocean and signifying the differences in the atmospheric forcing. Vertically, both
791 indicated a net downward advection of heat in the Pacific Ocean at 300 m, but much stronger intensity in the OFES1
792 (different by around 0.7 W/m^2); this may be related to their different wind-forcing sources, as the downward heat
793 advection in the upper ocean was mainly from the wind-driven Ekman pumping in the subtropical gyres. Indeed,
794 [Kutsuwada et al. \(2019\)](#) claimed that the NCEP wind stress curl was too strong and caused overly strong Ekman
795 pumping. There was 0.150 W/m^2 more eastward heat advection through the water passage between the Australian
796 mainland and 64° S (P3 in Fig. 1a) in the OFES2. Although the MHA from the Southern Ocean to the Pacific Oceans
797 (P4) was of opposite sign in the two OFES datasets, the relatively small absolute value indicated that this difference

798 was slight. The Drake Passage (P5) is the major water passage through which heat is exchanged between the Pacific
799 and Atlantic Oceans. There was 0.108 W/m^2 more heat loss through the P5 into the Atlantic Ocean in the OFES1,
800 inferring a stronger ACC from the OFES1 in the upper ocean. The P7 and P8 connect the Pacific and the Indian
801 Oceans; the Indonesian Throughflow (ITF) flows through the P7. The MHA through the P7 was almost two times
802 stronger in the OFES2 than in the OFES1, with a difference of 0.637 W/m^2 . This indicated an enhancement of the IFT
803 simulated by the OFES2, which agreed well with [Sasaki et al. \(2018\)](#), who showed that the inclusion of a tidal-mixing
804 scheme resulted in an intensification of the ITF, remembering that the a tidal-mixing scheme was implemented in the
805 OFES2 but not OFES1. In addition, the OFES1 showed more heat transported westward into the Indian Ocean between
806 Papua New Guinea and Australia (P8) but the small absolute heat advection indicated that it was not the major cause
807 of the OHC discrepancy between the OFES1 and OFES2. The net heat advection through the Bering Strait (P9) was
808 rather weak in both datasets. The indirect calculation of the VHD showed that there was net downward heat diffusion
809 at a depth of 300 m in the Pacific Ocean in both the two OFES datasets but with a much stronger intensity (different
810 by 0.747 W/m^2) in the OFES1.

811 In the Atlantic Ocean, the OHC increased at an average rate of 0.032 W/m^2 in the OFES1 but decreased by 0.014
812 W/m^2 in the OFES2. There was net surface heating in the OFES1 Atlantic Ocean but minor cooling in the OFES2.
813 The two OFES datasets were also profoundly different in the VHA at 300 m. Specifically, the OFES1 showed a net
814 downward heat advection, the OFES2 an upward and much weaker heat advection. Again, this difference in the VHA
815 was likely the result of different wind stress datasets in the two OFES, as discussed above. The OFES1 showed 0.158
816 W/m^2 more heat transported from the Atlantic Ocean to the Indian Ocean through the P1 between the South Africa
817 and 64° S . As mentioned above, more heat was advected into the Atlantic Ocean through the Drake Passage (P5) in
818 the OFES1. Additionally, there was more heat advected southward from the Atlantic Ocean to the Southern Ocean in
819 the OFES1 (P6). The wide passage connecting the north Atlantic Ocean to the Arctic Ocean (P10) also served as the
820 major channel through which the Atlantic Ocean exchanged heat; the two OFES datasets gave similar heat loss. All
821 these differences combined led us to conclude that the respective values for the vertical heat diffusion at 300 m differed
822 by 0.411 W/m^2 (more upward heat diffusion in the OFES1).

823 In the Indian Ocean, the averaged OHC increasing rate was 0.009 W/m^2 higher in the OFES2 than in the OFES1.
824 The time-averaged surface heat flux in the OFES2 was 0.729 W/m^2 less than that in the OFES1. Both datasets showed
825 a net downward heat advection but that in the OFES2 was around three times stronger. The small difference in the
826 southward heat advection across the 64° S (the P2) only affected the OHC in the upper Indian Ocean to a small extent.
827 In contrast, the differences in the HF, VHA and the MHA associated with the ITF contributed to the difference and
828 led us to calculate a remarkable discrepancy of 1.898 W/m^2 in the VHD at a depth of 300 m in the Indian Ocean. The
829 enhanced ITF is one of the main contributors to the larger OHC increase in the upper layer of the OFES2 Indian Ocean
830 (Fig. 2).

831 To summarize, there was generally more surface heat flux into the major basins in the OFES1. The vertical heat
832 advection was generally downward, indicating the essential role of the subtropical Ekman pumping in the heat uptake
833 in the upper ocean layer. The differences of these two (HF and VHA) were mainly from the different atmospheric
834 forcing used in the two OFES datasets, emphasizing the importance of reliable atmospheric forcing product in the

835 numerical ocean modelling. Although the different wind stress could also produce different lateral advectons through
 836 the P1–P10, the local-integrated differences were generally smaller than the basin-integrated differences. The most
 837 prominent difference in the lateral heat advection was associated with the ITF, mainly as a result of the adoption of a
 838 tidal-mixing scheme. This ITF-related difference and the indirectly inferred VHD suggested the significance of
 839 vertical mixing scheme in producing the examined differences of OHC.

840
 841 **Table 2.** Time-averaged OHC, surface heat flux (HF) and advection of heat through the major water passages for the upper layer
 842 of each basin (0–300 m). VHA is at a depth of 300 m. Residual: difference between the OHC increase and all the heat flux into a
 843 basin, approximately the vertical diffusion of heat. All quantities converted to W/m^2 applied over the entire surface of the Earth.
 844 Values smaller than 0.001 are set to 0. Positive means heat gain and negative means heat loss.

PACIFIC OCEAN (0–300 m)										
	OHC	HF	VHA	P3	P4	P5	P7	P8	P9	Residual
OFES1	–0.025	2.135	–0.814	1.233	0.011	–0.891	–0.728	–0.162	–0.003	–0.808
OFES2	0.007	1.066	–0.113	1.383	–0.020	–0.783	–1.365	–0.100	0	–0.061
ATLANTIC OCEAN (0–300 m)										
	OHC	HF	VHA	P1	P5	P6	P10	Residual		
OFES1	0.032	0.184	–0.445	–0.823	0.891	–0.085	–0.440	0.749		
OFES2	–0.014	–0.036	0.005	–0.665	0.783	–0.051	–0.388	0.338		
INDIAN OCEAN (0–300 m)										
	OHC	HF	VHA	P1	P2	P3	P7	P8	Residual	
OFES1	0.026	0.195	–0.639	0.823	–0.038	–1.233	0.728	0.162	0.028	
OFES2	0.035	–0.534	–2.091	0.665	–0.012	–1.383	1.365	0.100	1.926	

845
 846 *Middle layer*
 847 There were no significant differences between the OFES1 and OFES2 in the horizontal and vertical heat transports in
 848 the middle layer (300–700 m) of the Pacific Ocean (Tab. 3). It can be seen that the IFT was weak for this depth layer
 849 and its differences between the OFES1 and OFES2 was small ($0.084 W/m^2$). However, heat was advected or diffused
 850 from the upper layer (at 300 m, the top face of the middle ocean layer). There was a difference of around $0.747 W/m^2$
 851 in the VHD at a depth of 300 m in the Pacific Ocean and a difference of $0.701 W/m^2$ in the VHA. All these together
 852 led us to infer a VHD difference of $1.295 W/m^2$ at a depth of 700 m in the Pacific Ocean, with more heat was diffused
 853 downward in the OFES1.

854 In the Atlantic Ocean, the averaged OHC trend was positive in the OFES1 but negative in the OFES2, different by
 855 $0.129 W/m^2$. A VHA of $-1.585 W/m^2$ was calculated for the OFES2, 32% stronger than that for the OFES1.
 856 Additionally, more heat was lost through the P1 into the Indian Ocean and more heat was advected into the Atlantic
 857 Ocean through the Drake Passage in the OFES1. Differences also existed in the heat advection between the Atlantic
 858 Ocean, and the Southern (P6) and the Arctic (P10) Oceans. The vertical heat transport (VHA + VHD) at the 300 m of
 859 the Atlantic Ocean (Tab. 2) was close from the two OFES data. The resulting inferred VHD through the depth of 700
 860 m in the Atlantic Ocean was upward in both datasets but $0.393 W/m^2$ stronger in the OFES2.

861 The averaged OHC trend in the Indian Ocean was weakly negative in both the OFES1 and OFES2. $0.142 W/m^2$
 862 more heat was advected downward at a depth of 700 m in the OFES2. Horizontally, $0.121 W/m^2$ more heat was

863 acquired from the Atlantic Ocean (through the P1) in the OFES1 but there were neglectable differences in the lateral
 864 heat transport through the others passages connecting the Indian Ocean with the other basins. The time-averaged VHD
 865 at 700 m in the Indian Ocean was 0.423 W/m² in the OFES1 and 1.083 W/m² in the OFES2.

866 To summarize, the notable cooling trend in the Pacific and Atlantic Ocean (Fig.3) from the OFES2 came mainly
 867 from the vertical heat transport (VHA + VHD) processes. For example, there was a net upward heat advection at 300
 868 m in the OFES2 Atlantic Ocean and a stronger downward heat advection at 700 m, as a result, more heat was lost
 869 vertically in the middle layer of the OFES2 Atlantic Ocean compared to the OFES1 Atlantic Ocean.

870

871 **Table 3.** As for Tab. 2 but for the middle layer (300–700 m). VHA is at a depth of 700 m.

PACIFIC OCEAN (300–700 m)									
	OHC	VHA	P3	P4	P5	P7	P8	P9	Residual
OFES1	0.017	-0.096	1.208	-0.026	-1.056	0.044	0	0	-1.679
OFES2	-0.034	-0.084	1.247	-0.030	-0.917	-0.040	0	0	-0.384
ATLANTIC OCEAN (300–700 m)									
	OHC	VHA	P1	P5	P6	P10	Residual		
OFES1	0.037	-1.203	-0.770	1.056	0.056	-0.057	1.260		
OFES2	-0.092	-1.585	-0.649	0.917	0.017	-0.102	1.653		
INDIAN OCEAN (300–700 m)									
	OHC	VHA	P1	P2	P3	P7	P8	Residual	
OFES1	-0.010	-0.519	0.770	-0.043	-1.208	-0.044	0	0.423	
OFES2	-0.013	-0.661	0.649	-0.043	-1.247	0.040	0	1.083	

872

873 *Lower layer*

874 Consistent with Fig. 4, the OFES2 showed cooling in the bottom (700–2000m) layer of each basin, but the OFES1 an
 875 overall warming (Tab. 4). In the Pacific Ocean, the VHA at 2000 m was downward and of similar magnitude in the
 876 two OFES datasets. Due to the vertical coherence of the ACC, there was intense eastward heat advection through the
 877 P3 and P5, even below 700 m, with the OFES2 showing greater advection. The horizontal heat advection through the
 878 P4 and P7 was relatively weak but again larger in the OFES2. For example, the MHA through the P7 was more than
 879 two times larger in the OFES2. In fact, more heat advected southward into the Indian Ocean through the ITF was
 880 found in all the ocean layers (the OFES1 showed a weakly northward heat advection in the middle layer). As a result
 881 of these differences, and the VHA and VHD at a depth of 700 m, we calculated a significant difference in the VHD
 882 between the two OFES datasets at a depth of 2000 m in the Pacific Ocean of around 1.252 W/m² in the downward
 883 direction.

884 Unlike at 2000 m in the Pacific Ocean, there was much stronger downward heat advection at 2000 m in the OFES2
 885 Atlantic Ocean. The dominant horizontal heat advectons were through the P1 and P5, with the OFES2 showing
 886 stronger heat advection at both the two passages. We calculated a downward heat diffusion at a depth of 2000 m of
 887 0.216 W/m² in the OFES1 Atlantic Ocean and an upward VHD of 0.383 W/m² in the OFES2 Atlantic Ocean.

888 In the Indian Ocean, the calculated downward heat advection was two times stronger in the OFES1; there were
889 also some moderate differences in the horizontal heat advection. The resulting VHD at 2000 m was upward in both
890 the OFES1 and OFES2, but much greater (by 0.455 W/m^2) in the latter.

891 To summarize, differences in the lateral heat advection through the major passages P1–P10 in the lower layer was
892 small, and the major drivers of the examined OHC differences between the OFES1 and OFES2 came largely from the
893 vertical heat transport (VHA + VHD), similar to the situation in the middle layer.

894

895 **Table 4.** As for Tab. 2 but for the lower layer (700–2000 m). VHA is at a depth of 2000 m.

PACIFIC OCEAN (700–2000 m)									
	OHC	VHA	P3	P4	P5	P7	P8	P9	Residual
OFES1	0.058	-0.126	0.951	-0.04 7	-1.12 0	-0.035	0	0	-1.341
OFES2	-0.037	-0.105	1.146	-0.08 0	-1.29 4	-0.082	0	0	-0.089
ATLANTIC OCEAN (700–2000 m)									
	OHC	VHA	P1	P5	P6	P10	Residual		
OFES1	0.014	-0.029	-0.97 4	1.120	0.066	0.105	-0.216		
OFES2	-0.013	-0.536	-1.05 9	1.294	0.003	-0.031	0.383		
INDIAN OCEAN (700–2000 m)									
	OHC	VHA	P1	P2	P3	P7	P8	Residual	
OFES1	0.007	-0.241	0.974	-0.03 3	-0.95 1	0.035	0	0.126	
OFES2	-0.018	-0.120	1.059	-0.05 2	-1.14 6	0.082	0	0.581	

896 **4 Conclusions and Discussion**

897 In this paper, we estimated the OHC from two eddy-resolution hindcast simulations, OFES1 and OFES2, with a major
898 focus on their differences. The global observation-based dataset EN4 acted as a reference. The main findings were as
899 follows.

900 1. Multi-decadal warming was clearly seen in most of the global ocean (0–2000 m), especially in the EN4 and
901 OFES1. The warming was mainly manifested as deepening of the neutral density surfaces (HV component), with a
902 lesser contribution from changes along the neutral surfaces (SP component) of regional importance.

903 2. Significant differences in the OHC (or potential temperature) were found between the OFES1 and OFES2; the
904 major causes for these were fourfold. Firstly, there was generally more net surface heat flux in the OFES1. Secondly,
905 the ITF was almost two times stronger in the OFES2, especially in the top 300 m. Thirdly, the differences in the
906 intensity of the vertical heat advection were large, particularly at 300 m in the Indian Ocean. Finally, remarkable
907 differences in the vertical heat diffusion were inferred.

908 Although we have detailed the OHC differences between the OFES1 and OFES2, and also analysed the horizontal
909 and vertical heat transports in an attempt to understand the causes of these differences, more work is needed to

910 improve. Firstly, a direct calculation of the vertical heat diffusion was desirable to have a more reliable and accurate
911 comparison between the two datasets. In addition, decomposing the vertical heat diffusion into tidal mixing and mixed-
912 layer vertical mixing is also an interesting topic and may help to isolate the effects of tidal mixing on the ocean state.
913 Besides, we expect to see a detailed comparison of the wind stress from these two datasets over this 57-year period.
914 This is inspired by the work of [Kutsuwada et al. \(2019\)](#) and our detection of the large differences in the vertical heat
915 advection. Considering the apparent differences of the SP between the OFES2 and the other two datasets, a
916 comprehensive comparison of salinity between both the OFES1 and OFES2 with observations were required. This
917 helped the community to determine their choice of datasets for their own research purposes.

918 One may argue that being not well spun-up may be the major cause for the identified differences between the
919 OFES2 with others, since that the OFES1 followed a 50-year climatological simulation. This is likely to be a cause.
920 However, large differences between the two OFES datasets remain in the temporal evolution of the global and basin
921 OHCs, even during the last two decades. In addition, for example, [S2020](#) found that the Azores Current was simulated
922 in the OFES2 in the initial two decades but disappeared after 1970. This, to some extent, weaken the spin-up argument,
923 but does not rule out the possibility. The OFES2 was not expected to be highly sensitive to the spin-up issue, as it
924 started with conditions from the OFES1. That said, there were indeed some improvements in the OFES2 for the recent
925 decades, for example, over 2005-2016 (not shown here). Two potential explanations are: firstly, the model was full
926 spun-up after a couple of decades of integration; secondly, improvements of the reanalysis atmospheric forcing data
927 contributed to the simulation improvements.

928 Finally, the OFES products, especially the OFES1, did capture some of the warming and cooling trends shown by
929 the EN4 and in the literature, despite their having no observational-based constraints. However, the clear differences
930 between the two OFES datasets and the EN4 suggest the importance of observational data in improving the hindcast
931 performance. The significant differences in the vertical heat diffusion between the two OFES datasets also suggest
932 that special attention should be given to validation of the vertical mixing scheme in future ocean modelling.

933

934 **Author contributions:** F.L conceived the study. All authors contributed to the details of study design. F.L conducted
935 the calculations and analysis. F.L drafted the manuscript; Z.L and X.H.W improved the writing.

936

937 **Acknowledgements:** This is publication No. 87 of the Sino-Australian Research Consortium for Coastal Management
938 (previously the Sino-Australian Research Centre for Coastal Management). This work was supported by the Key
939 Special Project for Introduced Talents Team of the Southern Marine Science and Engineering Guangdong Laboratory
940 (Guangzhou; GML2019ZD0210). The authors thank Dr Peter McIntyre for improving the manuscript. The authors
941 acknowledge public access to the data used in this paper from the UK Meteorological Office and the JAMSTEC.

942

943 **Code and data availability:** OFES1 and OFES2 are based on the MOM3, available at [https://github.com/mom-](https://github.com/mom-ocean/MOM3)
944 [ocean/MOM3](https://github.com/mom-ocean/MOM3). Code for decomposing the potential temperature: <http://www.teos-10.org/software.htm>. Original EN4
945 data: <https://www.metoffice.gov.uk/hadobs/en4/download-en4-2-1.html>. Original OFES1 temperature and salinity
946 data: http://apdrc.soest.hawaii.edu/dods/public_ofes/OfES/ncep_0.1_global_mmean. Due to a data security incident,

947 access to the OFES2 data has been temporarily suspended. The data and codes (including the publically available
948 scripts for completion) needed to reproduce the results of this paper are archived on Zenodo
949 (<https://doi.org/10.5281/zenodo.5205444>). The archived data are annual mean values calculated from the original data.

950 **References**

951 Abraham, J. P., Reseghetti, F., Baringer, M., Boyer, T., Cheng, L., Church, J., Domingues, C., Fasullo, J. T., Gilson,
952 J., Goni, G., Good, S., Gorman, J. M., Gouretski, V., Ishii, M., Johnson, G. C., Kizu, S., Lyman, J., MacDonald, A.,
953 Minkowycz, W. J., Moffitt, S. E., Palmer, M., Piola, A., Trenberth, K. E., Velicogna, I., Wijffels, S., and Willis, J.: A
954 review of global ocean temperature observations: implications for ocean heat content estimates and climate change,
955 *Rev. Geophys.*, 51, 450-483, doi.org/10.1002/rog.20022, 2013.

956 AchutaRao, K. M., Ishii, M., Santer, B. D., Gleckler, P. J., Taylor, K. E., Barnett, T. P., Pierce, D. W., Stouffer, R. J.,
957 and Wigley, T. M. L.: Simulated and observed variability in ocean temperature and heat content, *Proc. Natl. Acad.*
958 *Sci.*, 104, 10768-10773, doi.org/10.1073/pnas.0611375104, 2007.

960 Allison, L. C., Roberts, C. D., Palmer, M. D., Hermanson, L., Killick, R. E., Rayner, N. A., Smith, D. M., and Andrews,
961 M. B.: Towards quantifying uncertainty in ocean heat content changes using synthetic profiles, *Environ. Res. Lett.*,
962 14, 084037, doi.org/10.1088/1748-9326/ab2b0b, 2019.

964 Balmaseda, M. A., Trenberth, K. E., and Källén, E.: Distinctive climate signals in reanalysis of global ocean heat
965 content, *Geophys. Res. Lett.*, 40, 1754-1759, doi.org/10.1002/grl.50382, 2013.

967 Bindoff, N. L., and McDougall, T. J.: Diagnosing climate change and ocean ventilation using hydrographic data, *J.*
968 *Phy. Oceanogr.*, 24, 1137-1152, [doi.org/10.1175/1520-0485\(1994\)024<1137:DCCA0V>2.0.CO;2](https://doi.org/10.1175/1520-0485(1994)024<1137:DCCA0V>2.0.CO;2), 1994.

970 Carton, J. A., Chepurin, G. A. and Chen, L.: SODA3: A New Ocean Climate Reanalysis, *J. Climate.*, 31, 6967-6983,
971 <https://doi.org/10.1175/JCLI-D-18-0149.1>, 2018.

973 Banks, H. T., and Gregory, J. M.: Mechanisms of ocean heat uptake in a coupled climate model and the implications
974 for tracer based predictions of ocean heat uptake, *Geophys. Res. Lett.*, 33, L07608,
975 <https://doi.org/10.1029/2005GL025352>, 2006.

977 Carton, J. A., Chepurin, G., A. and Chen, L.: SODA3: A New Ocean Climate Reanalysis, *J. Climate.*, 31, 6967-6983,
978 <https://doi.org/10.1175/JCLI-D-18-0149.1>, 2018.

980 Carton, J. A., Penny, S. G., and Kalnay, E.: Temperature and salinity variability in the SODA3, ECCO4r3, and ORAS5
981 ocean reanalyses, 1993–2015, *J. Climate.*, 32, 2277-2293, doi.org/10.1175/JCLI-D-18-0605.1, 2019.

983 Chen, X., Yan, Y., Cheng, X., and Qi, Y.: Performances of seven datasets in presenting the upper ocean heat content
984 in the South China Sea, *Adv. Atmos. Sci.*, 30, 1331-1342, doi.org/10.1007/s00376-013-2132-1, 2013.

986
987 Cheng, L., Trenberth, K. E., Palmer, M. D., Zhu, J., and Abraham, J.: Observed and simulated full-depth ocean heat
988 content changes for 1970–2005, *Ocean Sci.*, 12, 925-935, doi.org/10.5194/os-12-925-2016, 2016.

989
990 Cheng, L., and Zhu, J.: Artifacts in variations of ocean heat content induced by the observation system changes.
991 *Geophys. Res. Lett.*, 41, 7276-7283, https://doi.org/10.1002/2014GL061881, 2014.

992
993 Church, J. A., White, N. J., and Arblaster, J. M.: Significant decadal-scale impact of volcanic eruptions on sea level
994 and ocean heat content, *Nature*, 438, 74-77, doi.org/10.1038/nature04237, 2005.

995
996 Curry, R., Dickson, B. and Yashayaev, I.: A change in the freshwater balance of the Atlantic Ocean over the past four
997 decades. *Nature*, 426, 826-829, https://doi.org/10.1038/nature02206, 2003.

998
999 Desbruyères, D., McDonagh, E. L., King, B. A., and Thierry, V.: Global and Full-Depth Ocean Temperature Trends
1000 during the Early Twenty-First Century from Argo and Repeat Hydrography, *J. Climate.*, 30, 1985-1997,
1001 doi.org/10.1175/JCLI-D-16-0396.1, 2017.

1002
1003 Desbruyeres, D., Purkey, S. G., Mcdonagh, E. L., Johnson, G. C. and King, B. A.: Deep and abyssal ocean warming
1004 from 35 years of repeat hydrography. *Geophys. Res. Lett.*, 43, 10356-10365, doi.org/10.1002/2016GL070413, 2016.

1005
1006 Dong, S., Garzoli, S., and Baringer, M.: The role of interocean exchanges on decadal variations of the meridional heat
1007 transport in the South Atlantic, *J. Phys. Oceanogr.*, 41, 1498-1511, doi.org/10.1175/2011JPO4549.1, 2011.

1008
1009 Durack, P. J., Gleckler, P. J., Landerer, F. W., and Taylor, K. E.: Quantifying underestimates of long-term upper-
1010 ocean warming, *Nat. Climate Change.*, 4, 999-1005, https://doi.org/10.1038/nclimate2389, 2014.

1011
1012 Du, Y., Qu, T., Meyers, G., Masumoto, Y., and Sasaki, H.: Seasonal heat budget in the mixed layer of the southeastern
1013 tropical Indian Ocean in a high-resolution ocean general circulation model, *J. Geophys. Res. Oceans.*, 110, C04012,
1014 doi.org/10.1029/2004JC002845, 2005.

1015
1016 Emery, W.: Water Types and Water Masses, *Encyclopedia of Ocean Sciences*, 4, 3179-3187,
1017 doi.org/10.1006/rwos.2001.0108, 2001.

1018
1019 Ernst, W. G.: *Earth systems: processes and issues*. Cambridge University Press, 2000.

1020
1021 Forget, G., Campin, J.-M., Heimbach, P., Hill, C. N., Ponte, R. M., and Wunsch, C.: ECCO version 4: an integrated
1022 framework for non-linear inverse modeling and global ocean state estimation, *Geosci. Model Dev.*, 8 (10), 3071–
1023 3104, doi:10.5194/gmd-8-3071-2015, 2015.

1024
1025 Fyfe, J.: Southern Ocean warming due to human influence, *Geophys. Res. Lett.*, 33, L19701, 10.1029/2006GL027247,
1026 2006.

1027

1028 Gleckler, P. J., Santer, B. D., Domingues, C. M., Pierce, D. W., Barnett, T. P., Church, J. A., Taylor, K. E., Achutarao,
1029 K., Boyer, T. P., and Ishii, M.: Human-induced global ocean warming on multidecadal timescales, *Nat. Climate*
1030 *Change.*, 2, 524-529, doi.org/10.1038/nclimate1553, 2012.

1031
1032 Good, S. A., Martin, M., and Rayner, N. A.: EN4: Quality controlled ocean temperature and salinity profiles and
1033 monthly objective analyses with uncertainty estimates, *J. Geophys. Res. Oceans.*, 118, 6704-6716,
1034 doi.org/10.1002/2013JC009067, 2013.

1035
1036 Häkkinen, S., Rhines, P. B. and Worthen, D. L.: Heat content variability in the North Atlantic Ocean in ocean
1037 reanalyses, *Geophys. Res. Lett.*, 42, doi.org/10.1002/2015GL063299, 2901-2909, 2015.

1038
1039 Häkkinen, S., Rhines, P. B., and Worthen, D.: Warming of the global ocean: Spatial structure and water-mass trends,
1040 *J. Climate.*, 29, 4949-4963, doi.org/10.1175/JCLI-D-15-0607.1, 2016.

1041
1042 IPCC.: *Climate Change 2013: The Physical Science Basis*. Cambridge University Press, 1535pp.,
1043 doi:10.1017/CBO9781107415324, 2013.

1044
1045 Jackett, D. R., and McDougall, T. J.: A neutral density variable for the world's oceans, *J. Phys. Oceanogr.*, 27, 237-
1046 263, doi.org/10.1175/1520-0485(1997)027<0237:ANDVFT>2.0.CO;2, 1997.

1047
1048 Jayne, S. R., and Laurent, L. C. St.: Parameterizing tidal dissipation over rough topography, *Geophys. Res. Lett.*, 28,
1049 811-814, doi.org/10.1029/2000GL012044, 2001.

1050
1051 Kalnay, E., Kanamitsu, M., Kistler, R., Collins, W., Deaven, D., Gandin, L., Iredell, M., Saha, S., White, G., Woollen,
1052 J., Zhu, Y., Chelliah, M., Ebisuzaki, W., Higgins, W., Janowiak, J., Mo, K. C., Ropelewski, C., Wang, J., Leetmaa,
1053 A., Reynolds, R., Jenne, R., and Joseph, D.: The NCEP/NCAR 40-year reanalysis project, *B. Am. Meteorol. Soc.*,
1054 77, 437-472, doi.org/10.1175/1520-0477(1996)077<0437:TNYRP>2.0.CO;2, 1996.

1055
1056 Kutsuwada, K., Kakiuchi, A., Sasai, Y., Sasaki, H., Uehara, K., and Tajima, R.: Wind-driven North Pacific Tropical
1057 Gyre using high-resolution simulation outputs, *J. Oceanogr.*, 75, 81-93, 10.1007/s10872-018-0487-8, 2019.

1058
1059 Large, W. G., McWilliams, J. C., and Doney, S. C.: Oceanic vertical mixing: A review and a model with a nonlocal
1060 boundary layer parameterization, *Rev. Geophys.*, 32, 363-403, doi.org/10.1029/94RG01872, 1994.

1061
1062 Lee, S., Park, W., Baringer, M. O. A., Gordon, L., Huber, B. A., and Liu, Y.: Pacific origin of the abrupt increase in
1063 Indian Ocean heat content during the warming hiatus, *Nature Geosci.*, 8, 445-449, doi.org/10.1038/ngeo2438, 2015.

1064
1065 Levitus, S., Antonov, J. I., Boyer, T. P., Baranova, O., Garcia, H. E., Locarnini, R. A., Mishonov, A. V., Reagan, J.
1066 R., Seidov, D., and Yarosh, E. S.: World ocean heat content and thermocline sea level change (0–2000 m), *Geophys.*
1067 *Res. Lett.*, 39, 1955-2010, doi.org/10.1029/2012GL051106, 2012.

1068

1069 Liang, X., Piecuch, C. G., Ponte, R. M., Forget, G., Wunsch, C., and Heimbach, P.: Change of the global ocean vertical
1070 heat transport over 1993–2010, *J. Climate.*, 30, 5319-5327, doi.org/10.1175/JCLI-D-16-0569.1, 2017.

1071
1072 Liang, X., Liu, C. R., Ponte, M. and Chambers, D. P.: A Comparison of the Variability and Changes in Global Ocean
1073 Heat Content from Multiple Objective Analysis Products During the Argo Period, *J. Climate.*, 1-47,
1074 doi.org/10.1175/JCLI-D-20-0794.1, 2021.

1075
1076 Liu, C., Liang, X., Chambers, D. P. and Ponte, R. M.: Global Patterns of Spatial and Temporal Variability in Salinity
1077 from Multiple Gridded Argo Products, *J. Climate.*, 33, 8751-8766, <https://doi.org/10.1175/JCLI-D-20-0053.1>, 2020.

1078
1079 Liu, M., and T. Tanhua.: Water masses in the Atlantic Ocean: characteristics and distributions, *Ocean Sci.*, 17, 463-
1080 486, doi.org/10.5194/os-17-463-2021, 2021.

1081
1082 Noh, Y., and Kim, H. J.: Simulations of temperature and turbulence structure of the oceanic boundary layer with the
1083 improved near-surface process, *J. Geophys. Res. Oceans.*, 104, 15621-15634, doi.org/10.1029/1999JC900068, 1999.

1084
1085 O'Connor, B. M., Fine, R. A. and Olson, D. B.: A global comparison of subtropical underwater formation rates, *Deep*
1086 *Sea Research Part I: Oceanographic Research Papers*, 52, 1569-1590, doi.org/10.1016/J.DSR.2005.01.011, 2005.

1087
1088 Palmer, M. D., Mcneall, D. J., and Dunstone, N. J.: Importance of the deep ocean for estimating decadal changes in
1089 Earth's radiation balance, *Geophys. Res. Lett.*, 38, L13707, doi.org/10.1029/2011GL047835, 2011.

1090
1091 Pierce, D. W., Barnett, T. P., Achutarao, K., Gleckler, P. J., Gregory, J. M., and Washington, W. M.: Anthropogenic
1092 warming of the oceans: Observations and model results, *J. Climate.*, 19, 1873-1900, doi.org/10.1175/JCLI3723.1,
1093 2006.

1094
1095 Sasaki, H., Sasai, Y., Kawahara, S., Furuichi, M., Araki, F., Ishida, A., Yamanaka, Y., Masumoto, Y., and Sakuma,
1096 H.: A series of eddy-resolving ocean simulations in the world ocean-OFES (OGCM for the Earth Simulator) project,
1097 *Oceans '04 MTS/IEEE Techno-Ocean '04 (IEEE Cat. No. 04CH37600)* 3, 1535-1541, 2004.

1098
1099 Sasaki, H., Kida, S., Furue, R., Aiki, H., Komori, N., Masumoto, Y., Miyama, T., Nonaka, M., Sasai, Y., and Taguchi,
1100 B.: A global eddying hindcast ocean simulation with OFES2, *Geosci. Model Dev.*, 13, 3319-3336,
1101 doi.org/10.5194/gmd-13-3319-2020, 2020.

1102
1103 Smith, D. M., Allan, R.P., Coward, A.C., Eade, R., Hyder, P., Liu, C., Loeb, N.G., Palmer, M.D., Roberts, C.D. and
1104 Scaife, A.A.: Earth's energy imbalance since 1960 in observations and CMIP5 models, *Geophys. Res. Lett.*, 42, 1205-
1105 1213, doi.org/10.1002/2014GL062669, 2015.

1106
1107 Spence, P., Saenko, O. A., Sijp, W., and England, M.: The role of bottom pressure torques on the interior pathways of
1108 North Atlantic deep water, *J. Phys. Oceanogr.*, 42, 110-125, doi.org/10.1175/2011JPO4584.1, 2012.

1109

1110 St. Laurent, L. C., Simmons, H. L., and Jayne, S. R.: Estimating tidally driven mixing in the deep ocean, *Geophys.*
1111 *Res. Lett.*, 29, 21-21–21-24, doi.org/10.1029/2002GL015633, 2002.

1112
1113 Talley, L. D.: Shallow, Intermediate, and Deep Overturning Components of the Global Heat Budget, *J. Phys.*
1114 *Oceanogr.*, 33, 530-560, [https://doi.org/10.1175/1520-0485\(2003\)033<0530:SIADOC>2.0.CO;2](https://doi.org/10.1175/1520-0485(2003)033<0530:SIADOC>2.0.CO;2), 2003.

1115
1116 Trenberth, K. E., Fasullo, J. T., Von Schuckmann, K., and Cheng, L.: Insights into Earth's energy imbalance from
1117 multiple sources, *J. Climate.*, 29, 7495-7505, doi.org/10.1175/JCLI-D-16-0339.1, 2016.

1118
1119 Tsujino, H., Urakawa, S., Nakano, H., Small, R. J., Kim, W. M., Yeager, S. G., Danabasoglu, G., Suzuki, T., Bamber,
1120 J. L., Bentsen, M., Böning, C. W., Bozec, A., Chassignet, E. P., Curchitser, E., Boeira Dias, F., Durack, P. J., Griffies,
1121 S. M., Harada, Y., Ilicak, M., Josey, S. A., Kobayashi, C., Kobayashi, S., Komuro, Y., Large, W. G., Le Sommer, J.,
1122 Marsland, S. J., Masina, S., Scheinert, M., Tomita, H., Valdivieso, M., and Yamazaki, D.: JRA-55 based surface
1123 dataset for driving ocean-sea-ice models (JRA55-do), *Ocean Model.*, 130, 79-139,
1124 doi.org/10.1016/j.ocemod.2018.07.002, 2018.

1125
1126 Von Schuckmann, K., Palmer, M. D., Trenberth, K. E., Cazenave, A., Chambers, D. P., Champollion, N., Hansen, J.,
1127 Josey, S. A., Loeb, N. G., and Mathieu, P. P.: An imperative to monitor Earth's energy imbalance, *Nat. Climate*
1128 *Change.*, 6, 138-144, doi.org/10.1038/nclimate2876, 2016.

1129
1130 Wang, G., Cheng, L., Abraham, J., and Li, C.: Consensuses and discrepancies of basin-scale ocean heat content
1131 changes in different ocean analyses, *Clim. Dyn.*, 50, 2471-2487, doi.org/10.1007/s00382-017-3751-5, 2018.

1132
1133 Wang, X. H., Bhatt, V., and Sun, Y.-J.: Study of seasonal variability and heat budget of the East Australian Current
1134 using two eddy-resolving ocean circulation models, *Ocean. Dyn.*, 63, 549-563, doi.org/10.1007/s10236-013-0605-5,
1135 2013.

1136
1137 Wunsch, C.: The decadal mean ocean circulation and Sverdrup balance, *J. Mar. Res.*, 69, 417-434, doi.org/
1138 10.1357/002224011798765303, 2011.

1139
1140 Zanna, L., Khatiwala, S., Gregory, J. M., Ison, J., and Heimbach, P.: Global reconstruction of historical ocean heat
1141 storage and transport, *Proc. Natl. Acad. Sci.*, 116, 1126-1131, doi.org/10.1073/pnas.1808838115, 2019.

1142
1143 Zhang, Y., Feng, M., Du, Y. H., Phillips, E., Bindoff, N. L., and McPhaden, M. J.: Strengthened Indonesian
1144 Throughflow Drives Decadal Warming in the Southern Indian Ocean, *Geophys. Res. Lett.*, 45, 6167-6175,
1145 doi.org/10.1029/2018GL078265, 2018.

1146
1147
1148
1149
1150